Microscale modeling of rate-dependent failure in thermoplastic composites under off-axis loading

Kovacevic, Dragan ; Sundararajan, Bharath K.; van der Meer, Frans P.

DOI
10.1016/j.engfracmech.2022.108884

Publication date
2022

Document Version
Final published version

Published in
Engineering Fracture Mechanics

Citation (APA)
Kovacevic, D., Sundararajan, B. K., & van der Meer, F. P. (2022). Microscale modeling of rate-dependent failure in thermoplastic composites under off-axis loading. *Engineering Fracture Mechanics*, *276*(Part B), Article 108884. https://doi.org/10.1016/j.engfracmech.2022.108884

Engineering Fracture Mechanics 276 (2022) 108884

Contents lists available at ScienceDirect

Engineering Fracture Mechanics

journal homepage: www.elsevier.com/locate/engfracmech

Microscale modeling of rate-dependent failure in thermoplastic composites under off-axis loading

Dragan Kovačević [a,c,*], Bharath K. Sundararajan [b,c], Frans P. van der Meer [a]

[a] Delft University of Technology, Faculty of Civil Engineering and Geosciences, PO Box 5048, 2600 GA Delft, The Netherlands
[b] University of Twente, Faculty of Engineering Technology, PO Box 217, 7522 LW, Enschede, The Netherlands
[c] Dutch Polymer Institute (DPI), PO Box 902, 5600 AX, Eindhoven, The Netherlands

ARTICLE INFO

Dataset link: https://doi.org/10.4121/20065976.v1

Keywords:
Unidirectional composites
Strain-rate
Viscoplasticity
Microcracking
Finite deformations

ABSTRACT

In this paper we develop a finite deformation micromechanical framework for modeling rate-dependent failure in unidirectional composites under off-axis loading. The model performance is compared with original experiments on thermoplastic carbon/PEEK composites tested at different strain-rates and off-axis angles. To achieve quantitative agreement with the experiments, a microcrack initiation criterion based on the local stress and the local rate of deformation state in the polymer matrix is proposed. Microcracking is represented by a cohesive zone model, with special attention to the inclusion of geometric nonlinearity in the formulation. In this regard, the cohesive geometric nonlinearity is based on extension of an existing formulation to three-dimensional space. Beside microcracking, the Representative Volume Element (RVE) also accounts for viscoplasticity in the polymer matrix. A recently introduced dedicated arclength control method is utilized to impose a strain-rate on the micromodel. Accordingly, kinematic relations governing the RVE deformation allow for the change in orientation of the micromodel in the loading process. This change in orientation of the microstructure has an important implication on the apparent material strength.

1. Introduction

Continuous fiber reinforced polymer (FRP) composites are used in many load-carrying applications that require high performance, especially in the transportation industry. They offer the possibility for a substantial reduction in weight of structural components and better resistance to corrosion compared to metallic alternatives [1]. In addition to this, thermoplastic composites provide an opportunity for welding, and also recycling by melting the material. However, the melting process limits the viscosity of the material such that thermoplastics are not immediately suitable for large structures, when the resin cannot be pushed through the whole component even applying high pressures [1]. Furthermore, the viscous nature of the polymer matrix and the inherent heterogeneous structure of FRP composites make prediction of the material behavior under the time-dependent loading conditions a rather difficult task.

Historically, different scales of observation have been utilized in modeling the mechanical response of composites. Many studies to predict failure of the material have been conducted on the ply level or mesoscale where the polymer matrix and carbon fibers are represented in a homogenized way, making this approach computationally efficient. Classical mesoscale failure theories that account for interaction between different homogenized stress components in a ply are those by Azzi and Tsai [2] that led to definition of

---

[*] Corresponding author at: Delft University of Technology, Faculty of Civil Engineering and Geosciences, PO Box 5048, 2600 GA Delft, The Netherlands.
E-mail addresses: d.kovacevic-1@tudelft.nl (D. Kovačević), b.k.sundararajan@utwente.nl (B.K. Sundararajan), f.p.vandermeer@tudelft.nl (F.P. van der Meer).

https://doi.org/10.1016/j.engfracmech.2022.108884
Received 22 July 2022; Received in revised form 10 October 2022; Accepted 13 October 2022

the Tsai–Hill failure criterion, and by Tsai and Wu [3], which are frequently used to this date. Hashin and Rotem [4] realized the necessity to distinguish between fiber and matrix failure that gave rise to failure-mode-based criteria. Following this idea new theories have been proposed including that by Puck and Schürmann [5] and Dávila et al. [6]. Camanho et al. [7] introduced a three-dimensional (3D) invariant-based failure criteria where the preferred material directions are accounted for by means of structural tensors. Once defined, mesoscale failure criteria can be readily used in laminate analysis of different composite systems. However, one general issue with mesoscale formulations is the difficulty to explicitly include additional physical influences such as strain-rate effects in a failure criterion.

On the other hand, micromechanical modeling offers more information about the material structure and, therefore, a more suitable environment to develop physics-based models, although this advantage comes along with higher computational cost. Regarding material failure, by means of microscale simulations the ply level failure criteria may be checked and refined or new theories can be proposed. In this way, Sun et al. [8] derived failure envelopes from Representative Volume Element (RVE) simulations along with a comparison with classical mesoscale failure theories. Totry et al. [9] compared micromechanical failure prediction with experiments on a carbon/polyetheretherketone (C/PEEK) system subjected to transverse compression and longitudinal shear [10]. Vaughan and McCarthy [11] introduced a micromechanical model to study fracture under transverse shear and normal loading. Sharma et al. [12] showed that an RVE model calibrated at uniaxial loading cases is able to predict biaxial failure of a lamina. An image-based RVE from an actual microstructure was developed by Bhuiyan et al. [13] to examine the effect of geometrical features such as the distribution and morphology of fibers on the biaxial transverse strength. A new rate- and temperature-dependent material model for polymers was proposed by Bai et al. [14], and applied to analysis of kink band formation under longitudinal compression of a composite material. In a multiscale reduced order modeling approach Gao et al. [15] incorporated the RVE microstructure in predicting failure of a 10° off-axis composite laminate. The rate- and temperature-dependent failure under transverse tension of unidirectional (UD) composites was studied by Sato et al. [16] and compared with the three-point bending experiments.

The majority of the micromechanical modeling does not account for an arbitrary off-axis loading of the composite material. Exceptions among the mentioned papers are the work of Bai et al. [14] and Gao et al. [15], but they do not consider different strain-rates in the failure process. Govaert et al. [17] do account for rate-dependent failure under an arbitrary off-axis loading, but on a regular distribution of fibers inside the matrix and with a failure criterion based on a local equivalent shear strain in a single point in the micromodel.

In this paper we develop a 3D micromechanical framework for modeling off-axis failure in UD composites subjected to a prescribed strain-rate. The model is defined in the finite deformation framework, accounting for viscoplasticity in the matrix, as well as for microcracking by means of a cohesive zone (CZ) model. The geometrically nonlinear formulation for the cohesive zones is based on the work of Reinoso and Paggi [18], which is generalized to 3D. Cohesive segments are added on the fly [19], when a microcrack initiation criterion is satisfied. A new initiation criterion is proposed based on the local stress and the local rate of deformation in the polymer matrix. A constant global strain-rate is imposed on the RVE following kinematic relations introduced by Kovačević and Van der Meer [20], that are in accordance with the finite deformation requirement of the model. The model behavior is compared with experimental results on a UD C/PEEK composite system, exposed to a range of strain-rates at different off-axis angles and room temperature conditions. The nearly homogeneous stress states in these tests allows for direct comparison between the experimental response and results obtained from single scale micromechanical simulations up to failure.

The developed framework is envisioned to contribute to better understanding of the long-term behavior of thermoplastic composites. In the first place, the model estimates failure of the material under rate-dependent off-axis loading. Potentially the RVE can also be used in multiscale simulations to take the place of mesoscale constitutive models.

The layout of the paper is as follows: the experimental benchmark is introduced in the next section. Then the requirements of a microscale analysis are defined, followed by the homogenized kinematics description of the RVE. After that, the variational formulation of the equilibrium equation is presented, with special attention for the linearization of the cohesive contribution to the internal force vector. The explanation of constitutive models used to represent the polymer matrix and the carbon fibers follows. Subsequently a mixed-mode damage cohesive law is introduced, together with the microcrack initiation criterion. Next, the simulation results are compared with the experiment and the paper ends with some concluding remarks.

2. Experimental benchmark

The micromechanical modeling of the rate-dependent failure is compared with experiments on UD C/PEEK composite material. Carbon fiber reinforced UD tapes with PEEK matrix, specifically made for this research work, were provided by Solvay. The tapes were 103 mm wide with a nominal thickness of 0.25 mm. Previous work suggested that using commercial UD tapes with a higher fiber volume ratio leads to high variation in experimental results [21]. Hence, to have better repeatability in data, tapes with the fiber volume ratio $V_f = 0.4$ with more matrix than in commercial UD tapes were prepared. The quoted V_f of 0.4 was also verified by microscopy and measuring the fiber weight after burning off the resin in consolidated laminates. UD composite laminates were prepared from these tapes using the Pinette P.E.I press at the ThermoPlastic composites Research Centre (TPRC) in a two stage process.

UD plies of 390 × 390 mm dimensions were prepared from the prepreg tapes and were stacked in $[0]_{4s}$ layup. They were then placed between 1 mm thick stainless steel caul sheets, coated with Marbocote 227CEE release agent, in a picture frame. The plies were first heated to 385 °C (beyond the melting temperature of PEEK) at a rate of 5 °C/min under 2 bar pressure. The consolidation process was then carried out for 20 min under a pressure of 20 bar. Finally, the consolidated laminate was cooled down to room temperature at a uniform cooling rate of 5 °C/min.

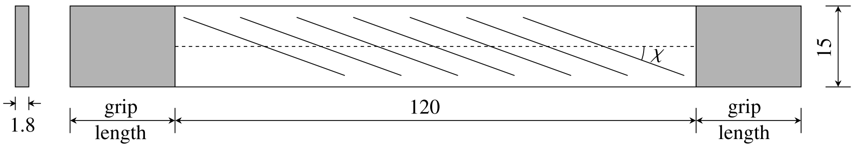

Fig. 1. Schematic representation of test coupons used for uniaxial tension experiments; all dimensions are in mm.

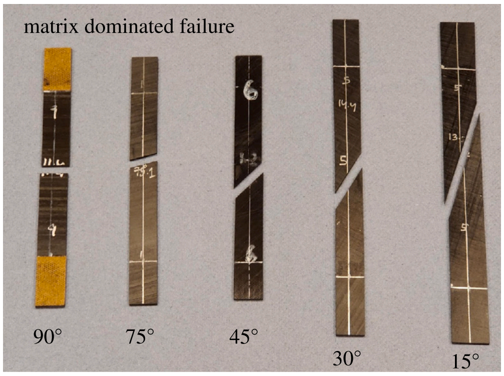

Fig. 2. Fractured UD composite laminates for different off-axis angles.

The consolidated laminates were cut into 4 smaller laminates of 190 × 190 mm dimension. They were then heated using an IR oven to 400 °C in 2 min and flat formed between 2 flat steel plates maintained at 175 °C, in order to isothermally crystallize the PEEK matrix. The flat formed laminates were then manually cut to rectangular tensile test coupons using a diamond saw. Water was used as a coolant to prevent any heating during the cutting process. The test coupons have a gauge length of 120 mm, width of 15 mm and thickness of 1.8 mm, as shown in Fig. 1, with grip length of either 20 mm or 25 mm depending on the clamp type. Sandpaper tabs were used to avoid failure in the clamping region. χ is the angle between the fibers and loading direction, which is often referred to as the off-axis angle.

A Zwick Z100 universal tensile tester equipped with a 50 kN load cell was used to perform the experiments. Constant strain-rate experiments on off-axis UD test coupons were performed at room temperature using constant crosshead speeds corresponding to strain-rates ranging between 10^{-6}/s and 10^{-3}/s. A clip-on extensometer with a gauge length of 25 mm was used to record the stress–strain relationship for some specimens. Specifically, the extensometer was used for all the experiments performed on 90° loaded samples, whereas at other loading angles it was used only at the strain-rate of 10^{-4}/s. The exception is $\chi = 15°$ in which case the extensometer was never used. A set of the broken specimens is shown in Fig. 2, indicating a matrix-dominated failure mechanism with a straight crack parallel to the fibers for all off-axis angles. The authors acknowledge that the rectangular shape of specimens in combination with the gripping effect will cause global inhomogeneity in the deformation for off-axis angles other than 90°. This effect could be monitored using Digital Image Correlation (DIC) [22], but that was not part of this study. An alternative approach to alleviate the potential inhomogeneity in the specimen response would be the application of the oblique end tabs [23].

3. Micromechanical framework

The RVE model aims at simulating failure of UD composite material under a constant strain-rate as depicted in Fig. 3, such that failure of the micromodel corresponds to the macroscopic crack formation. The micromodel is defined in the local coordinate system aligned with the fibers, providing that one side is parallel to the reinforcement. This allows for representing three-dimensional stress states in a micromodel of only a thin slice of the material. There is no restriction on the strain magnitude in the material, meaning that the local coordinate frame may change orientation from the angle $\theta_0 = 90° - \chi$ to a new angle θ_1, see Fig. 3. The state of the micromodel must be equivalent to the deformation and stress state of the material shown in Fig. 3. This means that in a homogenized sense the stresses acting on the RVE, see Fig. 4(left), must be equal to the Cauchy stresses in Fig. 3(right), and the deformation pattern of the RVE should correspond to the strain-rate applied in the global y-direction. In order to satisfy these requirements, a dedicated strain-rate based arclength formulation was derived [20]. The detailed derivation of the model is presented in [20], while here only the main equations are summarized.

3.1. Homogenized kinematics

An RVE with periodic boundary conditions is considered [24]. Kinematic relations are calculated from displacements on the master nodes of the RVE. The active master node displacements are shown in Fig. 4(right), accompanied by the unit force components

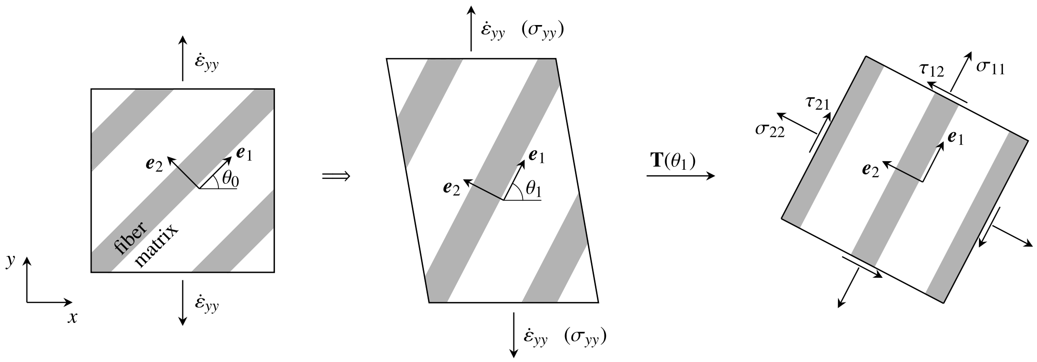

Fig. 3. Constant strain-rate applied on unidirectional composite material (left); finite deformation of the material (middle); Cauchy stress components in local coordinate system (right).

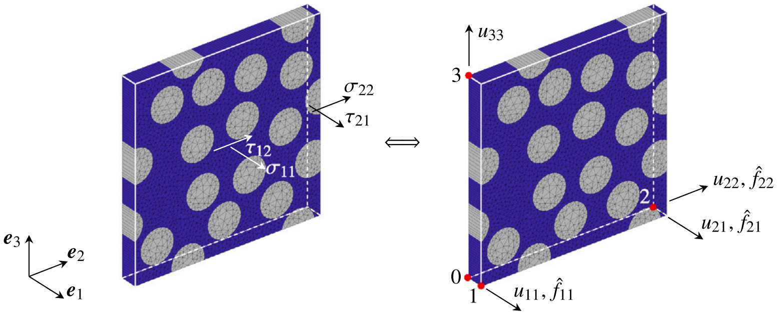

Fig. 4. Homogenized stress state of the RVE (left); active displacements and applied unit force components on master nodes of the RVE (right).

of the arclength model. Master node displacements not indicated in the figure are fully restrained. With such defined boundary conditions, the homogenized deformation gradient of the RVE is:

$$\bar{\mathbf{F}} = \begin{bmatrix} \bar{F}_{11} & \bar{F}_{12} & 0 \\ 0 & \bar{F}_{22} & 0 \\ 0 & 0 & \bar{F}_{33} \end{bmatrix} = \begin{bmatrix} 1+\frac{u_{11}}{l_1^0} & \frac{u_{21}}{l_2^0} & 0 \\ 0 & 1+\frac{u_{22}}{l_2^0} & 0 \\ 0 & 0 & 1+\frac{u_{33}}{l_3^0} \end{bmatrix} \tag{1}$$

where u_{ij} is the displacement on master node i in direction j and l_i^0 is the initial length of the RVE in direction i. The constraint equation of the arclength control method enforces that the RVE deforms according to the strain-rate prescribed in the analysis:

$$\left(1+\frac{u_{11}}{l_1^0}\right)s_0 s_1 + \left(1+\frac{u_{22}}{l_2^0}\right)c_0 c_1 + \frac{u_{21}}{l_2^0}c_0 s_1 - \exp(\varepsilon_{yy}^{n-1} + \dot{\varepsilon}_{yy}\Delta t) = 0 \tag{2}$$

In this equation s_i and c_i stand for $\sin(\theta_i)$ and $\cos(\theta_i)$ respectively, where i is either 0 or 1. The new angle θ_1, see Fig. 3, is calculated as $\theta_1 = \theta_0 + \phi$, in which the angle ϕ represents the change in orientation of the RVE due to the finite deformation and is defined as:

$$\phi = \arctan\left(\frac{-\bar{F}_{11}c_0 s_0 + \bar{F}_{12}s_0^2 + \bar{F}_{22}c_0 s_0}{\bar{F}_{11}c_0^2 - \bar{F}_{12}c_0 s_0 + \bar{F}_{22}s_0^2}\right) \tag{3}$$

In order to maintain a uniaxial stress state in the material at finite strains, the unit force vector of the arclength method is updated accordingly:

$$\begin{aligned} \hat{f}_{11} &= A_1^0 \bar{J}\left(\frac{s_1^2}{\bar{F}_{11}} - c_1 s_1 \frac{\bar{F}_{12}}{\bar{F}_{11}\bar{F}_{22}}\right) \\ \hat{f}_{21} &= A_2^0 \bar{J}\frac{c_1 s_1}{\bar{F}_{22}} \\ \hat{f}_{22} &= A_2^0 \bar{J}\frac{c_1^2}{\bar{F}_{22}} \end{aligned} \tag{4}$$

Here, A_i^0 is the initial surface of the RVE on which a corresponding stress component is acting, and $\bar{J}$ is the determinant of the RVE homogenized deformation gradient, Eq. (1). When multiplied with the load factor λ of the arclength method, the unit force components produce the desired homogenized stress state in the RVE, see Fig. 4. For this problem, the load factor is the same as the applied stress in the global loading direction, i.e., $\lambda = \sigma_{yy}$. Eventually, the simulation is performed on the RVE as depicted in Fig. 4(right), following the analysis steps as explained in [20].

3.2. Variational formulation

In this section the equilibrium equation between the internal and external force vector of a cracked body in the finite deformation framework is derived. The presence of cracks in the body is accounted for by means of a cohesive surface methodology. Special attention is dedicated to accurately represent geometric nonlinear effects of the cohesive zone. This problem has been treated in the literature in different contexts. Wells et al. [25] derived necessary equations in the XFEM framework to model delamination in laminated composites. Zhi et al. [26] tackled the problem of matrix cracking and delamination in composites and included the CZ geometric nonlinearity in the floating node method. In this work the CZ geometric nonlinearity is based on the idea introduced by Ortiz and Pandolfi [27], and further elaborated for 2D problems by Reinoso and Paggi [18]. We extend the work of Reinoso and Paggi [18] to 3D.

The virtual work of a cracked body, neglecting the body forces, can be written in the reference configuration as:

$$\int_{\Omega_0} (\nabla_{\mathbf{X}} \delta \mathbf{u}) : \mathbf{P} d\Omega_0 + \int_{\Gamma_{c0}} \delta [\![\mathbf{u}]\!] \cdot \mathbf{t}_0 d\Gamma_0 = \int_{\Gamma_{u0}} \delta \mathbf{u} \cdot \mathbf{t}_{p0} d\Gamma_0 \tag{5}$$

where $\delta\mathbf{u}$ is the virtual displacement, $\mathbf{P}$ is the first Piola–Kirchhoff stress, $\mathbf{t}_0$ is the nominal traction acting on a cohesive surface, $\delta[\![\mathbf{u}]\!]$ is the virtual displacement jump of the cohesive zone, and $\mathbf{t}_{p0}$ is the nominal traction prescribed on the boundary of the body. $\nabla_{\mathbf{X}}$ represents the gradient operator with respect to the initial coordinates $\mathbf{X}$. In order to derive the equilibrium equation between the internal end external forces in the current configuration, Eq. (5) is pushed forward. First, $\mathbf{P}$ is written as the product of the deformation gradient $\mathbf{F}$ and the second Piola–Kirchhoff stress $\mathbf{S}$:

$$\int_{\Omega_0} (\nabla_{\mathbf{X}} \delta \mathbf{u}) : (\mathbf{F}\mathbf{S}) d\Omega_0 + \int_{\Gamma_{c0}} \delta [\![\mathbf{u}]\!] \cdot (\mathbf{F}\mathbf{S}\mathbf{n}_0) d\Gamma_0 = \int_{\Gamma_{u0}} \delta \mathbf{u} \cdot \mathbf{t}_{p0} d\Gamma_0 \tag{6}$$

in which the nominal traction on the cohesive surface is replaced with $\mathbf{t}_0 = \mathbf{P}\mathbf{n}_0 = \mathbf{F}\mathbf{S}\mathbf{n}_0$, $\mathbf{n}_0$ being the vector normal to the cohesive surface in the initial configuration. The following relations from e.g. [25] are considered:

$$\begin{aligned} \nabla_{\mathbf{X}} \delta \mathbf{u} &= (\nabla_{\mathbf{x}} \delta \mathbf{u}) \mathbf{F} \\ \mathbf{n}_0 &= \frac{1}{\det(\mathbf{F})} \mathbf{F}^{\mathrm{T}} \mathbf{n} \frac{d\Gamma}{d\Gamma_0} \\ d\Omega_0 &= \frac{1}{\det(\mathbf{F})} d\Omega \end{aligned} \tag{7}$$

where $\nabla_{\mathbf{x}}$ is the gradient operator with respect to the deformed coordinates $\mathbf{x}$, and $\mathbf{n}$ is the normal vector in the current configuration. After substituting Eq. (7) in Eq. (6) and recognizing the relation between the Cauchy stress $\boldsymbol{\sigma}$ and $\mathbf{S}$ of the form:

$$\boldsymbol{\sigma} = \frac{1}{\det(\mathbf{F})} \mathbf{F}\mathbf{S}\mathbf{F}^{\mathrm{T}} \tag{8}$$

the virtual work of the system in the current configuration emerges as:

$$\int_{\Omega} (\nabla_{\mathbf{x}} \delta \mathbf{u}) : \boldsymbol{\sigma} d\Omega + \int_{\Gamma_c} \delta [\![\mathbf{u}]\!] \cdot (\boldsymbol{\sigma}\mathbf{n}) d\Gamma = \int_{\Gamma_u} \delta \mathbf{u} \cdot \mathbf{t}_p d\Gamma \tag{9}$$

The further derivation is expressed in Voigt notation, and the current traction on the cohesive surface $\mathbf{t} = \boldsymbol{\sigma}\mathbf{n}$, such that:

$$\int_{\Omega} (\nabla_{\mathbf{x}} \delta \mathbf{u})^{\mathrm{T}} \boldsymbol{\sigma} d\Omega + \int_{\Gamma_c} \delta [\![\mathbf{u}]\!]^{\mathrm{T}} \mathbf{t} d\Gamma = \int_{\Gamma_u} \delta \mathbf{u}^{\mathrm{T}} \mathbf{t}_p d\Gamma \tag{10}$$

The displacement field is discretized by means of the following relation:

$$\mathbf{u} = \mathbf{N}\mathbf{a} \tag{11}$$

where $\mathbf{N}$ is the shape function matrix, and $\mathbf{a}$ is the vector of nodal displacements. Similarly, the displacement jump is defined as:

$$[\![\mathbf{u}]\!] = \tilde{\mathbf{N}}\mathbf{a} = \begin{bmatrix} \mathbf{N}_{cz} & -\mathbf{N}_{cz} \end{bmatrix} \begin{bmatrix} \mathbf{a}_{\mathrm{top}} \\ \mathbf{a}_{\mathrm{bottom}} \end{bmatrix} \tag{12}$$

where $\mathbf{N}_{cz}$ is the shape function matrix defined over the cohesive surface, while the vector of nodal displacements is partitioned in the part corresponding to the top and bottom bulk finite elements of the cohesive zone, see Fig. 5. Upon transformation of the displacement jump from global to local frame of reference by means of the transformation matrix $\mathbf{Q}$, the displacement jump in local frame is written as:

$$[\![\bar{\mathbf{u}}]\!] = \mathbf{Q}\tilde{\mathbf{N}}\mathbf{a} \tag{13}$$

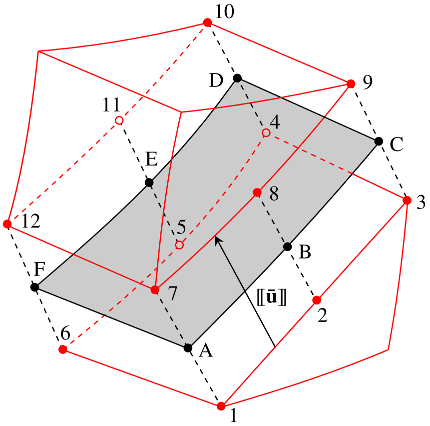

Fig. 5. Wedge-shaped bulk finite elements in decohesion process defined by displacement jump $[\![\bar{\mathbf{u}}]\!]$; cohesive segment represented as mid-surface between the two bulk elements.

Replacing Eqs. (11) and (12) in Eq. (10) in terms of their virtual counterparts, and expressing the cohesive zone contribution by means of the quantities defined in local frame, the discretized weak equilibrium equation in the current configuration becomes:

$$\int_{\Omega} [\nabla_{\mathrm{x}} \delta(\mathbf{N}\mathbf{a})]^{\mathrm{T}} \boldsymbol{\sigma} \, d\Omega + \int_{\Gamma_{\mathrm{c}}} \delta(\mathbf{Q}\tilde{\mathbf{N}}\mathbf{a})^{\mathrm{T}} \bar{\mathbf{t}} \, d\Gamma = \int_{\Gamma_{\mathrm{u}}} \delta(\mathbf{N}\mathbf{a})^{\mathrm{T}} \mathbf{t}_{\mathrm{p}} \, d\Gamma \tag{14}$$

where $\bar{\mathbf{t}}$ is the current cohesive traction in local coordinate system. Taking the first variation of Eq. (14) with respect to virtual nodal displacements yields the following expression:

$$\delta\mathbf{a}^{\mathrm{T}} \int_{\Omega} (\nabla_{\mathrm{x}} \mathbf{N})^{\mathrm{T}} \boldsymbol{\sigma} \, d\Omega + \delta\mathbf{a}^{\mathrm{T}} \int_{\Gamma_{\mathrm{c}}} \left(\mathbf{Q}\tilde{\mathbf{N}} + \frac{\partial \mathbf{Q}}{\partial \mathbf{a}} \tilde{\mathbf{N}}\mathbf{a} \right)^{\mathrm{T}} \bar{\mathbf{t}} \, d\Gamma = \delta\mathbf{a}^{\mathrm{T}} \int_{\Gamma_{\mathrm{u}}} \mathbf{N}^{\mathrm{T}} \mathbf{t}_{\mathrm{p}} \, d\Gamma \tag{15}$$

which holds for any kinematically admissible variation in the nodal displacements $\delta\mathbf{a}$. Therefore:

$$\int_{\Omega} (\nabla_{\mathrm{x}} \mathbf{N})^{\mathrm{T}} \boldsymbol{\sigma} \, d\Omega + \int_{\Gamma_{\mathrm{c}}} \left(\mathbf{Q}\tilde{\mathbf{N}} + \frac{\partial \mathbf{Q}}{\partial \mathbf{a}} \tilde{\mathbf{N}}\mathbf{a} \right)^{\mathrm{T}} \bar{\mathbf{t}} \, d\Gamma = \int_{\Gamma_{\mathrm{u}}} \mathbf{N}^{\mathrm{T}} \mathbf{t}_{\mathrm{p}} \, d\Gamma \tag{16}$$

This equation represents the equilibrium between the internal and external forces:

$$\mathbf{f}^{\mathrm{int}}_{\mathrm{bulk}} + \mathbf{f}^{\mathrm{int}}_{\mathrm{cz}} = \mathbf{f}^{\mathrm{ext}} \tag{17}$$

where the internal force vector consists of two parts. The bulk part is:

$$\mathbf{f}^{\mathrm{int}}_{\mathrm{bulk}} = \int_{\Omega} (\nabla_{\mathrm{x}} \mathbf{N})^{\mathrm{T}} \boldsymbol{\sigma} \, d\Omega = \int_{\Omega} \mathbf{B}^{\mathrm{T}} \boldsymbol{\sigma} \, d\Omega \tag{18}$$

in which $\mathbf{B}$ is the strain-nodal displacement matrix. The CZ part is:

$$\mathbf{f}^{\mathrm{int}}_{\mathrm{cz}} = \int_{\Gamma_{\mathrm{c}}} \left(\mathbf{Q}\tilde{\mathbf{N}} + \frac{\partial \mathbf{Q}}{\partial \mathbf{a}} \tilde{\mathbf{N}}\mathbf{a} \right)^{\mathrm{T}} \bar{\mathbf{t}} \, d\Gamma \tag{19}$$

Compared to the small displacement theory that would only account for the material contribution, Eq. (19) also features the geometric contribution to the internal force vector. This geometric contribution emerges as a consequence of the change in the transformation matrix with nodal displacements.

3.3. Linearization

The computational framework for the RVE model is based on the updated Lagrangian formulation [28]. Accordingly, the linearization can be done in the initial reference configuration, where the volume (or the cohesive surface) does not depend on the displacement field. Subsequently, in every iteration the current configuration is taken as the reference for the linearization, while all quantities are computed with respect to the current coordinates. Hence, although the integration domain for the internal force is changing from one iteration to the next, linearization does not require an additional term that accounts for this change.

The linearization of the bulk internal force vector leads to the following expressions for the global tangent stiffness matrix [28]:

$$\mathbf{K}_{\mathrm{bulk}} = \frac{\partial \mathbf{f}^{\mathrm{int}}_{\mathrm{bulk}}}{\partial \mathbf{a}} = \mathbf{K}^{\mathrm{mat}}_{\mathrm{bulk}} + \mathbf{K}^{\mathrm{geo}}_{\mathrm{bulk}} \tag{20}$$

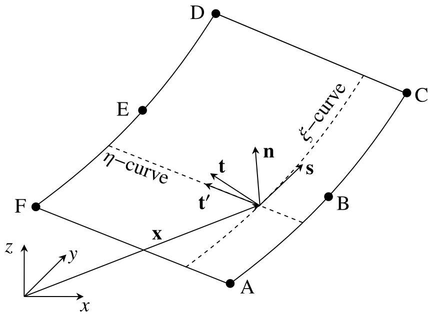

Fig. 6. **n**, **s**, **t** orthonormal vector triad derived from unit vectors **s** and **t**′ in direction of parametric curves ξ and η, respectively.

where the material contribution to the tangent stiffness is:

$$\mathbf{K}_{\text{bulk}}^{\text{mat}} = \int_{\Omega} \mathbf{B}^{\mathrm{T}}\mathbf{C}\mathbf{B}\, d\Omega \tag{21}$$

with **C** being the bulk constitutive matrix in the deformed configuration. The geometric contribution to the tangent stiffness relating degrees of freedom of nodes I and J is:

$$\mathbf{K}_{\text{bulk},IJ}^{\text{geo}} = \mathbf{I}\int_{\Omega} \mathbf{B}_I^{\mathrm{T}}\boldsymbol{\sigma}\mathbf{B}_J\, d\Omega \tag{22}$$

where the quantity inside the integral is a scalar and **I** is the unit matrix.

The linearization of the CZ internal force vector is more involved and treated here in more detail. The CZ tangent stiffness matrix includes the material and the geometric part:

$$\mathbf{K}_{\text{cz}} = \frac{\partial \mathbf{f}_{\text{cz}}^{\text{int}}}{\partial \mathbf{a}} = \mathbf{K}_{\text{cz}}^{\text{mat}} + \mathbf{K}_{\text{cz}}^{\text{geo}} \tag{23}$$

The material part is defined as:

$$\mathbf{K}_{\text{cz}}^{\text{mat}} = \int_{\Gamma} \left(\mathbf{Q}\tilde{\mathbf{N}}\right)^{\mathrm{T}} \bar{\mathbf{T}}\mathbf{Q}\tilde{\mathbf{N}}\, d\Gamma \tag{24}$$

where $\bar{\mathbf{T}}$ is the material tangent stiffness operator that provides mapping between the displacement jump and the traction vector in the local frame. In the linearization process the second derivative of the transformation matrix with respect to nodal displacements is neglected. Therefore, the geometric part of the tangent stiffness comprises four terms:

$$\mathbf{K}_{\text{cz}}^{\text{geo}} = \mathbf{K}_{\text{g}1} + \mathbf{K}_{\text{g}2} + \mathbf{K}_{\text{g}3} + \mathbf{K}_{\text{g}4} \tag{25}$$

$$\begin{aligned}
\mathbf{K}_{\text{g}1} &= 2\int_{\Gamma} \left(\frac{\partial \mathbf{Q}}{\partial \mathbf{a}}\tilde{\mathbf{N}}\right)^{\mathrm{T}} \bar{\mathbf{t}}\, d\Gamma \\
\mathbf{K}_{\text{g}2} &= \int_{\Gamma} \left(\frac{\partial \mathbf{Q}}{\partial \mathbf{a}}\tilde{\mathbf{N}}\mathbf{a}\right)^{\mathrm{T}} \bar{\mathbf{T}}\frac{\partial \mathbf{Q}}{\partial \mathbf{a}}\tilde{\mathbf{N}}\mathbf{a}\, d\Gamma \\
\mathbf{K}_{\text{g}3} &= \int_{\Gamma} \left(\mathbf{Q}\tilde{\mathbf{N}}\right)^{\mathrm{T}} \bar{\mathbf{T}}\frac{\partial \mathbf{Q}}{\partial \mathbf{a}}\tilde{\mathbf{N}}\mathbf{a}\, d\Gamma \\
\mathbf{K}_{\text{g}4} &= \int_{\Gamma} \left(\frac{\partial \mathbf{Q}}{\partial \mathbf{a}}\tilde{\mathbf{N}}\mathbf{a}\right)^{\mathrm{T}} \bar{\mathbf{T}}\mathbf{Q}\tilde{\mathbf{N}}\, d\Gamma
\end{aligned} \tag{26}$$

To account for the CZ geometric contribution in both the internal force vector and the tangent stiffness matrix, it is necessary to compute the 3D array $\partial\mathbf{Q}/\partial\mathbf{a}$. For this, we need to express every component of **Q** in terms of nodal displacements. The transformation matrix derives from the orthonormal basis **n**, **s**, **t**, that is associated with any point of the cohesive surface, see Fig. 6, such that:

$$\mathbf{Q} = \begin{bmatrix} n_x & n_y & n_z \\ s_x & s_y & s_z \\ t_x & t_y & t_z \end{bmatrix} \tag{27}$$

Computationally, the cohesive surface is represented as a mid-surface between two adjacent bulk finite elements, involved in the decohesion process. Since the bulk elements are wedge-shaped with 12 nodes, in order to ensure the compatibility in the discretization, the cohesive element is also a 12-node element, connecting two 6-node quadrilateral faces, see Fig. 5. The position vector **x** of any node of the mid-surface in the current configuration points to the half-distance between two corresponding bulk nodes:

$$\begin{aligned} \mathbf{x}_\mathrm{A} &= \frac{1}{2}(\mathbf{x}_1 + \mathbf{x}_7), \quad & \mathbf{x}_\mathrm{D} &= \frac{1}{2}(\mathbf{x}_4 + \mathbf{x}_{10}) \\ \mathbf{x}_\mathrm{B} &= \frac{1}{2}(\mathbf{x}_2 + \mathbf{x}_8), \quad & \mathbf{x}_\mathrm{E} &= \frac{1}{2}(\mathbf{x}_5 + \mathbf{x}_{11}) \\ \mathbf{x}_\mathrm{C} &= \frac{1}{2}(\mathbf{x}_3 + \mathbf{x}_9), \quad & \mathbf{x}_\mathrm{F} &= \frac{1}{2}(\mathbf{x}_6 + \mathbf{x}_{12}) \end{aligned} \tag{28}$$

The utilized 6-node quadrilateral shape that parametrizes the mid-surface features the isoparametric formulation, such that the shape functions are defined in the parent $\xi - \eta$ coordinate system as follows:

$$\begin{aligned} N_\mathrm{A} &= \frac{1}{4}(1-\eta)(\xi^2 - \xi), \quad & N_\mathrm{D} &= \frac{1}{4}(1+\eta)(\xi^2 + \xi) \\ N_\mathrm{B} &= \frac{1}{2}(1-\eta)(1 - \xi^2), \quad & N_\mathrm{E} &= \frac{1}{2}(1+\eta)(1 - \xi^2) \\ N_\mathrm{C} &= \frac{1}{4}(1-\eta)(\xi^2 + \xi), \quad & N_\mathrm{F} &= \frac{1}{4}(1+\eta)(\xi^2 - \xi) \end{aligned} \tag{29}$$

Following the principles of the isoparametric formulation, the position vector of any point of the cohesive surface, see Fig. 6, emerges as:

$$\mathbf{x} = N_\mathrm{A}\mathbf{x}_\mathrm{A} + \cdots + N_\mathrm{F}\mathbf{x}_\mathrm{F} \tag{30}$$

Given the position vector in Eq. (30), it is possible to define the unit vectors associated with the parametrized directions ξ and η in the current configuration, see Fig. 6:

$$\mathbf{s} = \frac{\partial \mathbf{x}/\partial \xi}{\|\partial \mathbf{x}/\partial \xi\|} = \frac{\tilde{\mathbf{s}}}{\|\tilde{\mathbf{s}}\|} \tag{31}$$

$$\mathbf{t}' = \frac{\partial \mathbf{x}/\partial \eta}{\|\partial \mathbf{x}/\partial \eta\|} = \frac{\tilde{\mathbf{t}}'}{\|\tilde{\mathbf{t}}'\|} \tag{32}$$

With the unit vectors $\mathbf{s}$ and $\mathbf{t}'$, the unit vector normal to the cohesive surface is calculated as:

$$\mathbf{n} = \mathbf{s} \times \mathbf{t}' = \begin{bmatrix} s_y t'_z - s_z t'_y \\ s_z t'_x - s_x t'_z \\ s_x t'_y - s_y t'_x \end{bmatrix} \tag{33}$$

In the general deformation process the cohesive surface can be distorted such that the unit vectors $\mathbf{s}$ and $\mathbf{t}'$ are not perpendicular. In order to form the orthonormal basis, vectors $\mathbf{n}$ and $\mathbf{s}$ are employed to calculate the vector $\mathbf{t}$, see Fig. 6:

$$\mathbf{t} = \mathbf{n} \times \mathbf{s} = \begin{bmatrix} n_y s_z - n_z s_y \\ n_z s_x - n_x s_z \\ n_x s_y - n_y s_x \end{bmatrix} \tag{34}$$

In order to compute $\partial\mathbf{Q}/\partial\mathbf{a}$, it is necessary to find the derivative of every component of the transformation matrix, Eq. (27), with respect to nodal displacements:

$$\frac{\partial \mathbf{Q}}{\partial \mathbf{a}} = \begin{bmatrix} n_{x,\mathbf{a}} & n_{y,\mathbf{a}} & n_{z,\mathbf{a}} \\ s_{x,\mathbf{a}} & s_{y,\mathbf{a}} & s_{z,\mathbf{a}} \\ t_{x,\mathbf{a}} & t_{y,\mathbf{a}} & t_{z,\mathbf{a}} \end{bmatrix}_{3\times3\times36(\mathrm{ndof})} \tag{35}$$

A derivation of these derivatives is shown in Appendix.

4. Constitutive models

In this section the viscoplastic constitutive model used for the matrix is described. Then, the material model for carbon fibers is briefly outlined, and finally the cohesive law to represent microcracking in the matrix is introduced.

4.1. The Eindhoven Glassy Polymer constitutive model

In order to include viscous and plasticity effects in the polymer matrix we choose the Eindhoven Glassy Polymer (EGP) model. Unlike many material models used to represent inelastic behavior of engineering materials, the EGP does not feature a yield surface. Instead it follows the Eyring flow theory [29] to describe the deformation kinetics of polymer materials. In the EGP an Eyring-based viscosity function reduces as a consequence of the stress applied on the material, such that the plastic flow at yield is regarded as the stress induced melting [30]. In this paper, only equations needed to define the model parameters are shown, whereas an in depth derivation can be found in, e.g., [30,31].

The EGP is an isotropic, elasto-viscoplastic material model that accounts for the finite strains in polymer material. The model builds upon the multiplicative decomposition of the deformation gradient into the elastic and the plastic part:

$$\mathbf{F} = \mathbf{F}_\mathrm{e} \cdot \mathbf{F}_\mathrm{p} \tag{36}$$

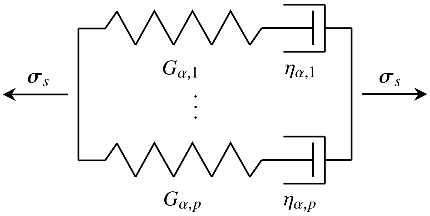

Fig. 7. Mechanical analog for a single process (α), multi-mode driving stress in the EGP model.

The change in volume is purely elastic, such that:

$$J = \det(\mathbf{F}) = \det(\mathbf{F}_{\mathrm{e}}) \tag{37}$$

The Cauchy stress is additively decomposed in three components:

$$\boldsymbol{\sigma} = \boldsymbol{\sigma}_{\mathrm{h}} + \boldsymbol{\sigma}_{\mathrm{r}} + \boldsymbol{\sigma}_{\mathrm{s}} \tag{38}$$

Here $\boldsymbol{\sigma}_{\mathrm{h}}$ is the hydrostatic stress, $\boldsymbol{\sigma}_{\mathrm{r}}$ the hardening stress, and $\boldsymbol{\sigma}_{\mathrm{s}}$ is the driving stress. The hydrostatic stress depends on the bulk modulus κ:

$$\boldsymbol{\sigma}_{\mathrm{h}} = \kappa(J-1)\mathbf{I} \tag{39}$$

where $\mathbf{I}$ is the second order unit tensor. The hardening stress is defined as [30]:

$$\boldsymbol{\sigma}_{\mathrm{r}} = G_{\mathrm{r}}\tilde{\mathbf{B}}^{\mathrm{d}} \tag{40}$$

in which G_{r} is the hardening modulus and $\tilde{\mathbf{B}}^{\mathrm{d}}$ is the isochoric, deviatoric, left Cauchy–Green deformation tensor:

$$\tilde{\mathbf{B}}^{\mathrm{d}} = \left(\tilde{\mathbf{F}}\cdot\tilde{\mathbf{F}}^{\mathrm{T}}\right)^{\mathrm{d}} = J^{-2/3}\left(\mathbf{F}\cdot\mathbf{F}^{\mathrm{T}}\right)^{\mathrm{d}} \tag{41}$$

The driving stress introduces viscoplasticity in the model. This stress component allows for thermorheologically complex behavior of the material, meaning that more than one relaxation process may govern the material response [32]. In the case of two relaxation processes, α and β, the driving stress reads:

$$\boldsymbol{\sigma}_{\mathrm{s}} = \boldsymbol{\sigma}_{\alpha} + \boldsymbol{\sigma}_{\beta} \tag{42}$$

However, in this paper only α process is considered, such that $\boldsymbol{\sigma}_{\mathrm{s}} = \boldsymbol{\sigma}_{\alpha}$. The α relaxation process is represented by a Maxwell model with shear modulus on the elastic spring and viscosity on the dashpot. In order to improve the accuracy in the pre-yield regime Van Bremen et al. [30] considered a spectrum of relaxation times. This way, the α process consists of a number of Maxwell elements connected in parallel, with different shear moduli and viscosities, see Fig. 7. Let $G_{\alpha,j}$ be the shear modulus of jth Maxwell element of the process α, and $\tilde{\mathbf{B}}^{\mathrm{d}}_{\mathrm{e}\alpha,j}$ be the elastic part of the isochoric, deviatoric left Cauchy–Green deformation tensor describing the deformation on spring of Maxwell element j. Then the driving stress is:

$$\boldsymbol{\sigma}_{\mathrm{s}} = \sum_{j=1}^{q}\boldsymbol{\sigma}_{\alpha,j} = \sum_{j=1}^{q} G_{\alpha,j}\tilde{\mathbf{B}}^{\mathrm{d}}_{\mathrm{e}\alpha,j} \tag{43}$$

with q the number of modes for the process α. In order to calculate $\tilde{\mathbf{B}}^{\mathrm{d}}_{\mathrm{e}\alpha,j}$ in Eq. (43), it is necessary to solve for $\tilde{\mathbf{B}}_{\mathrm{e}\alpha,j}$ by integrating the corresponding rate equation:

$$\dot{\tilde{\mathbf{B}}}_{\mathrm{e}\alpha,j} = \left(\tilde{\mathbf{L}} - \mathbf{D}_{\mathrm{p}\alpha,j}\right)\cdot\tilde{\mathbf{B}}_{\mathrm{e}\alpha,j} + \tilde{\mathbf{B}}_{\mathrm{e}\alpha,j}\cdot\left(\tilde{\mathbf{L}}^{\mathrm{T}} - \mathbf{D}_{\mathrm{p}\alpha,j}\right) \tag{44}$$

where $\tilde{\mathbf{L}}$ is the isochoric velocity gradient. At this point it is necessary to define a constitutive relation for the plastic part of the rate of deformation tensor in Eq. (44), which is introduced in the form of a non-Newtonian flow rule:

$$\mathbf{D}_{\mathrm{p}\alpha,j} = \frac{\boldsymbol{\sigma}_{\alpha,j}}{2\eta_{\alpha,j}(\bar{\tau}_{\alpha}, p, S_{\alpha})} \tag{45}$$

$\eta_{\alpha,j}$ is the viscosity of Maxwell element j. It depends on the equivalent stress $\bar{\tau}_{\alpha}$, the hydrostatic pressure $p = -\mathrm{tr}(\boldsymbol{\sigma})/3$, and the thermodynamic state parameter S_{α}:

$$\eta_{\alpha,j} = \eta_{0\alpha,j}\frac{\bar{\tau}_{\alpha}/\tau_{0\alpha}}{\sinh(\bar{\tau}_{\alpha}/\tau_{0\alpha})}\exp\left(\frac{\mu_{\alpha}p}{\tau_{0\alpha}}\right)\exp(S_{\alpha}) \tag{46}$$

where $\eta_{0\alpha,j}$ is the corresponding initial viscosity, $\tau_{0\alpha}$ is the characteristic shear stress, and μ_{α} is the pressure dependency parameter. The equivalent stress has the following form:

$$\bar{\tau}_{\alpha} = \sqrt{\frac{1}{2}\boldsymbol{\sigma}_{\alpha} : \boldsymbol{\sigma}_{\alpha}} \tag{47}$$

Table 1
Relaxation spectrum of the EGP model.

j	$G_{\alpha,j}$ [MPa]	$\eta_{0\alpha,j}$ [MPa·s]	j	$G_{\alpha,j}$ [MPa]	$\eta_{0\alpha,j}$ [MPa·s]
1	1045.52	$7.590 \cdot 10^{21}$	9	50.61	$9.198 \cdot 10^{10}$
2	400.03	$8.502 \cdot 10^{16}$	10	83.94	$2.272 \cdot 10^{10}$
3	46.06	$2.570 \cdot 10^{14}$	11	77.28	$8.756 \cdot 10^{8}$
4	87.28	$1.843 \cdot 10^{13}$	12	60.61	$2.874 \cdot 10^{7}$
5	72.43	$5.912 \cdot 10^{12}$	13	56.67	$1.127 \cdot 10^{6}$
6	63.03	$1.992 \cdot 10^{12}$	14	4.64	$3.851 \cdot 10^{4}$
7	45.46	$5.520 \cdot 10^{11}$	15	53.03	$1.840 \cdot 10^{3}$
8	42.43	$1.987 \cdot 10^{11}$	16	3.42	$4.961 \cdot 10^{1}$

Table 2
Material parameters of the EGP model.

κ [MPa]	G_{r} [MPa]	$\tau_{0\alpha}$ [MPa]	μ_α	$S_{\mathrm{a}\alpha}$	$r_{0\alpha}$	$r_{1\alpha}$	$r_{2\alpha}$
2600	14.2	1.386	0.08	3	0.95	1	−5

The state parameter S_α represents the thermodynamical history of the material as a function of the equivalent plastic strain $\bar{\gamma}_{\mathrm{p}}$:

$$S_\alpha(\bar{\gamma}_{\mathrm{p}}) = S_{\mathrm{a}\alpha} R_{\gamma\alpha}(\bar{\gamma}_{\mathrm{p}}) \tag{48}$$

It accounts for two interacting mechanisms: the physical aging $S_{\mathrm{a}\alpha}$ and mechanical rejuvenation modeled by the softening function $R_{\gamma\alpha}(\bar{\gamma}_{\mathrm{p}})$. While the aging process increases the yield stress of the material, the presence of mechanical load tends to reverse this process and bring it to the (mechanically) rejuvenated state. The softening function in the EGP model is a modified Carreau–Yasuda function [33]:

$$R_{\gamma\alpha}(\bar{\gamma}_{\mathrm{p}}) = \left\{ \frac{1 + [r_{0\alpha} \exp(\bar{\gamma}_{\mathrm{p}})]^{r_{1\alpha}}}{1 + r_{0\alpha}^{r_{1\alpha}}} \right\}^{\frac{r_{2\alpha}-1}{r_{1\alpha}}} \tag{49}$$

The equivalent plastic strain $\bar{\gamma}_{\mathrm{p}}$ in Eq. (49) is calculated by integrating the evolution law:

$$\dot{\bar{\gamma}}_{\mathrm{p}} = \frac{\bar{\tau}_{\alpha,1}}{\eta_{\alpha,1}}, \quad \bar{\tau}_{\alpha,1} = \sqrt{\frac{1}{2}\boldsymbol{\sigma}_{\alpha,1} : \boldsymbol{\sigma}_{\alpha,1}} \tag{50}$$

which depends on the equivalent stress and the viscosity of a mode with the highest initial viscosity, that is mode 1. The relaxation spectrum for the process α is presented in Table 1. The other material model parameters are specified in Table 2. The starting point to determine parameters in Tables 1 and 2 was the data set describing the behavior of PEEK obtained according to [30]. However, the corresponding relaxation spectrum led to inaccurate behavior of the composite RVE when compared with the experimental results. A reason for this inaccuracy might be a different crystallinity of neat polymer and the polymer matrix in the composite. Therefore, the original relaxation spectrum was modified as follows: the highest viscosity was calibrated to achieve the stress level corresponding to the plateau of the $\chi = 45°$ experiment at $\dot{\varepsilon}_{yy} = 10^{-4}$/s; the rest of the spectrum was shifted such that the nonlinear part prior to the plateau of the $\chi = 45°$ experiment is properly captured, resulting in the data shown in Table 1.

4.2. Transversely isotropic material model for carbon fibers

No failure is assumed to take place in the carbon fibers, therefore the reinforcement behaves elastically in the RVE. The material model chosen to describe the behavior of the fibers is the hyperelastic transversely isotropic constitutive model formulated by Bonet and Burton [34]. In this paper only the part of formulation related to the stress calculation is shown. The Cauchy stress is decomposed in an isotropic and a transversely isotropic stress contribution:

$$\boldsymbol{\sigma} = \boldsymbol{\sigma}_{\mathrm{iso}} + \boldsymbol{\sigma}_{\mathrm{tri}} \tag{51}$$

The isotropic stress tensor reads:

$$\boldsymbol{\sigma}_{\mathrm{iso}} = \frac{\mu}{J}(\mathbf{B} - \mathbf{I}) + \frac{\bar{\lambda}}{J}\ln(J)\mathbf{I} \tag{52}$$

This stress component slightly differs from the original paper [34] and is the same as in [20]. The transversely isotropic contribution is defined as:

$$\boldsymbol{\sigma}_{\mathrm{tri}} = J^{-1}\{2\beta(I_4 - 1)\mathbf{B} + 2[\alpha + \beta(I_1 - 3) + 2\gamma(I_4 - 1)]\boldsymbol{a} \otimes \boldsymbol{a} - \alpha(\mathbf{B}\boldsymbol{a} \otimes \boldsymbol{a} + \boldsymbol{a} \otimes \mathbf{B}\boldsymbol{a})\} \tag{53}$$

In Eqs. (52) and (53), $\mathbf{B}$ is the left Cauchy–Green deformation tensor, J is the determinant of the deformation gradient $\mathbf{F}$, and $\mathbf{I}$ is the second order unit tensor. The vector $\boldsymbol{a}$ is the preferential stiffness direction of the material in the deformed configuration,

Table 3
Material parameters of the transversely isotropic constitutive model.

E_1 [GPa]	E_2 [GPa]	G_{12} [GPa]	ν_{12}	ν_{23}
125	15	45	0.05	0.3

obtained as $\boldsymbol{a} = \mathbf{F}\boldsymbol{A}$, where $\boldsymbol{A}$ is the preferential stiffness direction in the initial configuration. The invariants I_1 and I_4 are defined as:

$$\begin{aligned} I_1 &= \mathrm{tr}(\mathbf{B}) \\ I_4 &= \boldsymbol{a}\cdot\boldsymbol{a} \end{aligned} \tag{54}$$

The other material parameters in Eqs. (52) and (53): $\bar{\lambda}$, μ, α, β, γ are adopted according to [20]:

$$\begin{aligned} n &= \frac{E_1}{E_2} \\ m &= 1 - \nu_{23} - 2n\nu_{12}^2 \\ \bar{\lambda} &= \frac{E_2(\nu_{23} + n\nu_{12}^2)}{m(1+\nu_{23})} \\ \mu &= \frac{E_2}{2(1+\nu_{23})} \\ \alpha &= \mu - G_{12} \\ \beta &= \frac{E_2(\nu_{12} + \nu_{23}\nu_{12} - \nu_{23} - n\nu_{12}^2)}{4m(1+\nu_{23})} \\ \gamma &= \frac{E_1(1-\nu_{23})}{8m} - \frac{\bar{\lambda}+2\mu}{8} + \frac{\alpha}{2} - \beta \end{aligned} \tag{55}$$

Here, E_1 is the Young's modulus in the preferential stiffness direction, G_{12} and ν_{12} are the shear modulus and Poisson's ratio in the planes perpendicular to the plane of isotropy, E_2 and ν_{23} are the elastic constants in the transverse plane. Values of these parameters are listed in Table 3. Note that G_{12} has a higher value than usually reported in the literature, e.g. [35]. This value is calibrated to provide a good match in the initial slope between the experiments and the RVE simulation.

4.3. Cohesive law

Microcracking in the matrix is represented by means of a cohesive surface methodology. Cohesive segments along element edges are added on the fly [19] whenever a microcrack initiation criterion is satisfied. As introduced in Section 2, the traction is acting on a cohesive surface as a function of the displacement jump, see Fig. 5. The relation between the traction and the displacement jump is provided by a mixed-mode damage cohesive law elaborated by Liu et al. [36]. The governing equations of the cohesive model are summarized here with the extension to 3D. Since cohesive elements are inserted on the fly, the cohesive traction should have a non-zero value at zero opening, see Fig. 8(left), where the normal component of the traction is plotted against the normal component of the displacement jump. The area under the graph is the fracture energy of the material G_c. Direct application of this kind of cohesive law under mixed-mode conditions would lead to a singularity [37]. To avoid working with an infinite initial stiffness, the cohesive law is evaluated by shifting the displacement jump $[\![\bar{\mathbf{u}}]\!]$ for a value depending on the magnitude of the jump at crack initiation as proposed by Hille et al. [38], see Fig. 8(middle):

$$[\![\bar{\mathbf{u}}]\!]^{\mathrm{sh}} = [\![\bar{\mathbf{u}}]\!] + [\![\bar{\mathbf{u}}]\!]^0 \tag{56}$$

The shift $[\![\bar{\mathbf{u}}]\!]^0$ is defined as:

$$[\![\bar{\mathbf{u}}]\!]^0 = \frac{\bar{\mathbf{t}}^0}{K_m} \tag{57}$$

where $\bar{\mathbf{t}}^0$ is the traction on the cohesive surface in the local frame at the instant of microcrack initiation, and $K_m = 10^6$ N/mm^3 is the initial dummy stiffness. In simulating rate-dependent failure, we assume that the magnitude of $\bar{\mathbf{t}}^0$ may depend on the local rate of deformation. The evolution of the traction with changing displacement jump is governed by the cohesive law through:

$$\bar{\mathbf{t}} = (\mathbf{I} - \boldsymbol{\Omega})K_m[\![\bar{\mathbf{u}}]\!]^{\mathrm{sh}} = (\mathbf{I} - \boldsymbol{\Omega})\bar{\mathbf{t}}^{\mathrm{eff}} \tag{58}$$

where $\mathbf{I}$ is the unit tensor and $\bar{\mathbf{t}}^{\mathrm{eff}}$ is the effective traction on the cohesive surface. The decohesion process is driven by the damage variable ω_m used to construct the damage tensor $\boldsymbol{\Omega}$:

$$\Omega_{ij} = \omega_m\delta_{ij}\left(1 + \delta_{i1}\frac{\langle -t_n^{\mathrm{eff}}\rangle}{t_n^{\mathrm{eff}}}\right) \tag{59}$$

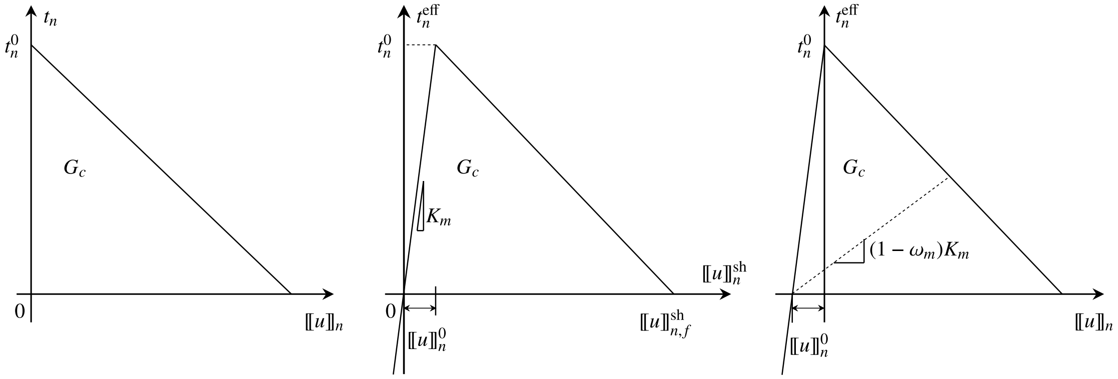

Fig. 8. Mode I representation of the shifted mixed-mode damage cohesive law.

Essentially, only the diagonal terms of $\boldsymbol{\Omega}$ are nonzero. The diagonal terms are equal to ω_m, except in the case of compression when the diagonal term corresponding with normal opening and traction vanishes. The evolution of the scalar damage variable ω_m is irreversible:

$$\omega_m = \max_{\tau \le t} \begin{cases} 0, & \Delta \le \Delta_0 \\ \frac{\Delta_f}{\Delta}\left(\frac{\Delta - \Delta_0}{\Delta_f - \Delta_0}\right), & \Delta_0 < \Delta < \Delta_f \\ 1, & \Delta > \Delta_f \end{cases} \tag{60}$$

where Δ is the shifted equivalent displacement jump:

$$\Delta = \left[(\langle [\![u]\!]_n^{\text{sh}} \rangle)^2 + ([\![u]\!]_s^{\text{sh}})^2 + ([\![u]\!]_t^{\text{sh}})^2\right]^{1/2} \tag{61}$$

In Eq. (60) Δ_0 is the equivalent displacement jump at the onset of failure:

$$\Delta_0 = \frac{t_{\text{eq}}^0}{K_m} \tag{62}$$

where t_{eq}^0 is the corresponding equivalent traction on the cohesive surface:

$$t_{\text{eq}}^0 = \left[(t_n^0)^2 + (t_s^0)^2 + (t_t^0)^2\right]^{1/2} \tag{63}$$

The degradation process is completed when the equivalent shifted displacement jump reaches a critical value Δ_f defined as:

$$\Delta_f = \frac{2G_c}{t_{\text{eq}}^0} \tag{64}$$

The unloading of the cohesive law is secant, with the slope depending on the current state of damage at an integration point, see Fig. 8(right). In the space of finite elements, the complete unloading happens when two neighboring bulk finite elements overlap for the value Δ_0, which is the consequence of the introduced shift when evaluating the cohesive law. Moreover, due to this shift, the actual energy dissipation during decohesion will be smaller than G_c. However, both the overlapping upon unloading and the reduction in effective energy dissipation vanish when K_m approaches infinity.

4.4. Microcrack initiation criterion

Before the cohesive law activates, a proper microcrack initiation criterion must be satisfied. In order to have quantitative comparison with the experiment, we propose an initiation criterion that is rate-dependent. First, at every time step the traction is computed on a potential cohesive surface, see Fig. 9, that is on any surface between finite elements of the matrix part or interface between the carbon fibers and the matrix. The traction is then decomposed in the components perpendicular and parallel to the fiber direction:

$$\begin{aligned} t_\perp &= \left(t_n^2 + t_s^2\right)^{1/2} \\ t_\parallel &= t_t \end{aligned} \tag{65}$$

The reason for this stress decomposition is the fact that for the off-axis angle of 90° the fracture process is completely governed by $t_\perp$, whereas $t_\parallel = 0$. On the other hand, for the lower off-axis angles, e.g. $\chi = 15°$, the stress component parallel with the fibers

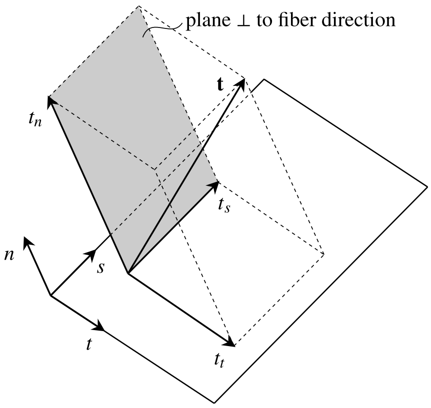

Fig. 9. Traction acting on a potential cohesive surface with corresponding stress components.

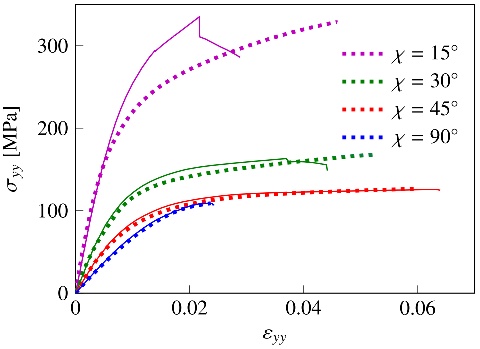

Fig. 10. Simulation results (solid) compared with experiment (dotted) at $\dot{\varepsilon}_{yy} = 10^{-4}$/s; one initiation envelope assumed for every point in matrix, and one initiation envelope assumed at matrix/fiber interface.

becomes more dominant and mostly drives the microcracking process. With these two stress components a power law initiation criterion is proposed in the following form:

$$\left(\frac{t_{\perp}}{f_{\perp}}\right)^{m} + \left(\frac{t_{\parallel}}{f_{\parallel}}\right)^{n} < 1 \tag{66}$$

where m and n are the constants, while $f_{\perp}$ and $f_{\parallel}$ are the strength parameters in the corresponding directions. An alternative approach, in which the stress vector is decomposed in the component normal to the cohesive surface t_n and shear component $t_{\text{sh}} = \left(t_s^2 + t_t^2\right)^{1/2}$ is also possible. This would lead to different calibration of the cohesive law, i.e., different initiation stress and fracture energies. Due to the possible misalignment of the cohesive surface normal and maximum principal stress, the t_s component is not necessarily equal to zero for a mode I fracture process.

In this study $n = 2$ was chosen to ensure the symmetry of the initiation criterion with respect to the shear stress $t_{\parallel}$, while $m = 3$ was calibrated to achieve a good estimate for the strain at failure for $\chi = 45°$ and a reasonably good estimate for $\chi = 30°$ off-axis angle. The change in coefficient m has much lower effect on the strain at failure for $\chi = 15°$, as compared for 30° and 45° loading angles. Further, the strain-rate $\dot{\varepsilon}_{yy} = 10^{-4}$/s is applied on the RVE with the fiber volume ratio $V_f = 0.4$. The calibrated strength values are: $f_{\perp} = 130$ MPa and $f_{\parallel} = 60$ MPa for matrix cracks and $f_{\perp} = 130$ MPa and $f_{\parallel}^{\text{if}} = 75$ MPa for fiber/matrix interface cracks. The simulation results for different off-axis angles are plotted in Fig. 10 and compared with the experiment. The onset of softening in the RVE response corresponds with macroscopic failure, and that point is used to make comparison with the experimental stress and strain at failure. The model qualitatively and quantitatively corresponds well with the experiment for the angles ranging from 30° to 90°, while for the angle of 15° there is an offset. In this case the simulation does match the observed stress at failure, but the strain at failure differs significantly. To achieve a similar level of accuracy for the strain-rates other than $\dot{\varepsilon}_{yy} = 10^{-4}$/s it proves necessary to change the strength parameters $f_{\perp}$ and $f_{\parallel}$. The initiation envelopes corresponding to different global strain-rates are shown in Fig. 11, for matrix and matrix/fiber interface, where the matrix/fiber interface strength $f_{\parallel}^{\text{if}} = 75$ MPa is kept constant.

This state of the initiation criteria is similar to the idea presented by Sato et al. [16]. They employ a unique initiation envelope according to the Christensen failure theory [39] for every global (macroscopic) strain-rate acting on the RVE. Accordingly, every point of the RVE has the same initiation envelope, irrespective of the possibly different local deformation rate. In this paper, we propose a microscopic initiation criterion based on the stress and the local rate of deformation state at any point of the RVE. To

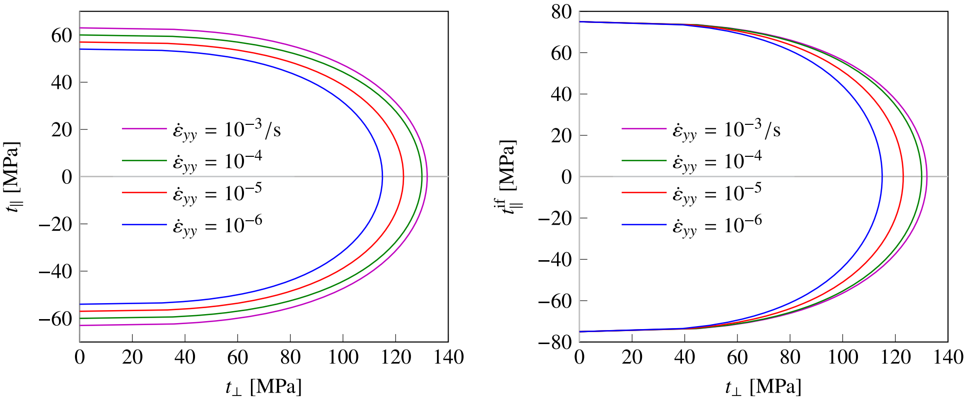

Fig. 11. Microcrack initiation envelopes for matrix (left) and matrix/fiber interface (right) for different strain-rates, according to Eq. (66).

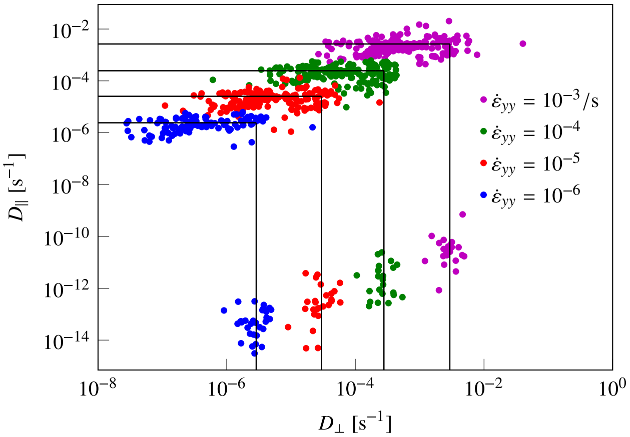

Fig. 12. Rate of deformation components computed when microcrack initiation criterion from Fig. 11 is satisfied for different strain-rates.

characterize the deformation rate, the rate of deformation tensor **D** is used, which is defined as the symmetric part of the velocity gradient **L**:

$$\mathbf{D} = \frac{1}{2}(\mathbf{L} + \mathbf{L}^{\mathrm{T}}) = \frac{1}{2}(\dot{\mathbf{F}}\mathbf{F}^{-1} + \mathbf{F}^{-\mathrm{T}}\dot{\mathbf{F}}^{\mathrm{T}}) \tag{67}$$

The reason for this choice is twofold. First, **D** is the work-conjugate to the Cauchy stress. Second, it is objective under a rigid-body rotation and follows the same transformation rule as the Cauchy stress [40], i.e.:

$$\bar{\mathbf{D}} = \mathbf{Q}\mathbf{D}\mathbf{Q}^{\mathrm{T}} \tag{68}$$

Therefore, together with the traction components on the potential cohesive surface, the corresponding rate of deformation components are also computed:

$$\begin{aligned} D_{\perp} &= \left(D_{nn}^2 + D_{ns}^2\right)^{1/2} \\ D_{\|} &= D_{nt} \end{aligned} \tag{69}$$

The RVE analyses have been repeated with the feature that every time an initiation criterion from Fig. 11 is met, the rate of deformation components are stored. Results are plotted in Fig. 12. It can be seen that the components $D_{\perp}$ and $D_{\|}$ form separate clouds of points in the rate of deformation space for every considered global strain-rate. This distinction in the local rate of deformation enables constructing different regions, such that the boundary of a region is parametrized with the $\dot{\varepsilon}_{yy}$ that defines a corresponding initiation envelope in Fig. 11. Each boundary is determined with a $D_{\perp}$ and a $D_{\|}$ component, which are listed in Table 4 together with the $\dot{\varepsilon}_{yy}$ parameter. The vertical lines in Fig. 12 represent the average value of the $D_{\perp}$ component calculated for $\chi = 90°$. The horizontal lines in the same figure correspond to the average value of the $D_{\|}$ component obtained from the simulations with off-axis angles of 15°, 30° and 45°. These angles are considered because the power law initiation parameters in Eq. (66) are calibrated from the corresponding off-axis experiments. In Fig. 12 there are also points from $\chi = 60°$ and $\chi = 75°$ simulations which oscillate around the corresponding horizontal lines, but are not included in defining the average values, although accounting for these points as well would not drastically change the outcome.

Table 4
The rate of deformation components defining boundaries in Fig. 12 and the strength values defining initiation envelopes in Fig. 11 corresponding to parameter $\dot{\varepsilon}_{yy}$.

$\dot{\varepsilon}_{yy}$ [s^{-1}]	$D_\perp$ [s^{-1}]	$D_\parallel$ [s^{-1}]	$f_\perp$ [MPa]	$f_\parallel$ [MPa]
10^{-6}	$2.88 \cdot 10^{-6}$	$2.42 \cdot 10^{-6}$	115	54
10^{-5}	$2.97 \cdot 10^{-5}$	$2.54 \cdot 10^{-5}$	123	57
10^{-4}	$2.78 \cdot 10^{-4}$	$2.46 \cdot 10^{-4}$	130	60
10^{-3}	$2.94 \cdot 10^{-3}$	$2.65 \cdot 10^{-3}$	132	63

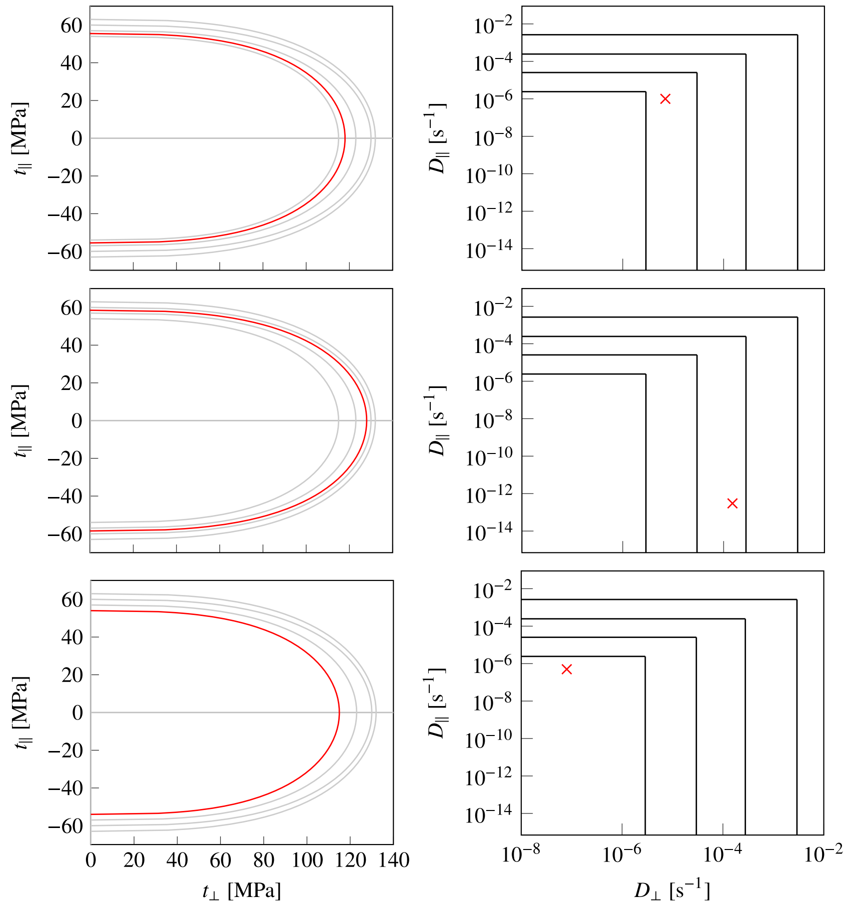

Fig. 13. Strategy to construct microcrack initiation envelope by interpolating between two neighboring parametric curves (left), depending on the local rate of deformation state (right).

As already stated, the $\dot{\varepsilon}_{yy}$ parametrizes the curves in Fig. 11, which are calculated from Eq. (66). The strength parameters adopted to construct these curves for different values of the $\dot{\varepsilon}_{yy}$ are also listed in Table 4. The strategy to compute the local initiation envelope for any potential cohesive surface is as follows:

1. compute components $D_\perp$ and $D_\parallel$ at a point of possible microcrack initiation
2. given $D_\perp$ and $D_\parallel$ find the equivalent loading rate $\dot{\varepsilon}_{yy}^{\max}$ from Table 4, linearly interpolating between the corresponding rate of deformation components; $\dot{\varepsilon}_{yy}^{(1)} = f(D_\perp)$, $\dot{\varepsilon}_{yy}^{(2)} = f(D_\parallel)$, $\dot{\varepsilon}_{yy}^{\max} = \max(\dot{\varepsilon}_{yy}^{(1)}, \dot{\varepsilon}_{yy}^{(2)})$
3. given $\dot{\varepsilon}_{yy}^{\max}$, compute $f_\perp$ and $f_\parallel$ from Table 4, linearly interpolating between the corresponding strength parameters; note that $f_\parallel^{\text{if}}$ always equals 75 MPa
4. given $f_\perp$ and $f_\parallel$, construct the initiation envelope using Eq. (66)

This strategy is illustrated in Fig. 13, where for a given point in the rate of deformation space the corresponding initiation envelope represents a proper interpolation between two adjacent parametric curves. If the point is outside the defined regions, the envelope is the closest parametric curve.

As part of this procedure we need to evaluate the rate of deformation tensor at the integration point level, Eq. (67). In the updated Lagrangian formulation followed in this paper, the deformation gradient from the previous time step $\mathbf{F}^{n-1}$ and the current

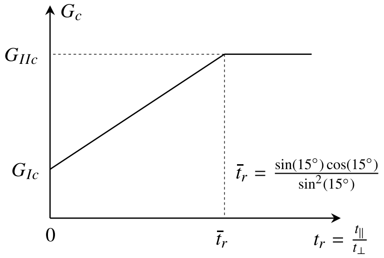

Fig. 14. Cohesive law fracture energy as function of local stress ratio at the moment of microcrack initiation.

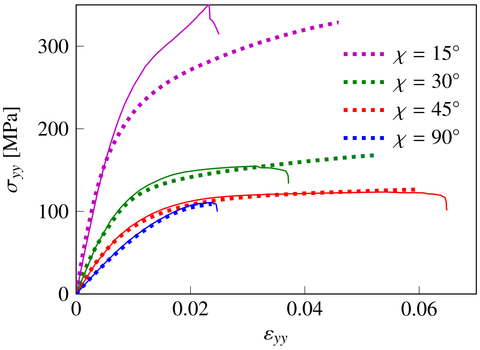

Fig. 15. Simulation (solid) versus experiment (dotted) for $\dot{\varepsilon}_{yy} = 10^{-4}$/s and different off-axis angles.

time step $\mathbf{F}^n$ are available at every integration point. Therefore the time derivative of $\mathbf{F}$ in Eq. (67) can be approximated:

$$\dot{\mathbf{F}} = \lim_{\Delta t \to 0} \frac{\Delta \mathbf{F}}{\Delta t} \approx \frac{\Delta \mathbf{F}}{\Delta t} = \frac{\mathbf{F}^n - \mathbf{F}^{n-1}}{\Delta t} \tag{70}$$

$\Delta \mathbf{F}$ in this equation should not be confused with an increment in the deformation gradient $d\mathbf{F}$ used to update the deformation gradient $\mathbf{F}^n = d\mathbf{F} \cdot \mathbf{F}^{n-1}$. In the case no additional deformation is present $\Delta \mathbf{F}$ is a zero tensor, while $d\mathbf{F}$ is a unit tensor.

Beside an initiation stress, the cohesive law also requires the fracture energy G_c as an input. The fracture mode changes with different off-axis angles, and the fracture mode likely influences the effective energy dissipation. To account for this, the G_c provided to the cohesive law interpolates between a lower bound value G_{Ic} calibrated for $\chi = 90°$, and an upper bound value G_{IIc} determined for $\chi = 15°$ at the strain-rate $\dot{\varepsilon}_{yy} = 10^{-4}$/s, see Fig. 14. The local value of G_c is determined when the cohesive segment is inserted and depends on the ratio $t_\parallel / t_\perp$ at initiation, which represents for these micromechanical simulations a sufficient insight in the mode, or degree of mode mixity of the fracture process. The quantity $\bar{t}_r$ in Fig. 14 is the initial ratio between the homogenized shear stress τ_{21} and normal stress σ_{22} acting on a plane parallel with the fiber direction when $\chi = 15°$, see Fig. 4. In this paper the following values are adopted: $G_{Ic} = 0.03$ N/mm, $G_{IIc} = 0.095$ N/mm, for all strain-rates and for matrix cracks and fiber/matrix interfacial cracks alike.

5. Results and discussion

In this section the performance of the RVE model is examined through comparison with the experimental benchmark. The stress σ_{yy} in the global loading direction, see Fig. 3, is plotted against the strain component ε_{yy}. The goal of this exercise is to illustrate capabilities of the model, without detailed statistical analysis on the size of the RVE. Therefore, the micromodel counting in total 9 fibers (3 × 3) of the diameter $D_f = 5$ μm is considered. A single set of parameters describing the rate and the stress dependent initiation as outlined in the previous section is considered in every simulation. As for the experiments, in the cases when the extensometer was not used to measure the exact strain, an empirically determined coefficient of 0.8 multiplies the experimental strain to cancel the compliance effect.

The RVE model has been subjected to the strain-rate of $\dot{\varepsilon}_{yy} = 10^{-4}$/s under different off-axis angles. In Fig. 15 the simulation results are plotted against the experimental measurements. It can be seen from the figure that the results obtained with the rate-dependent initiation criterion are similar to those obtained earlier with fixed initiation criterion calibrated for this strain-rate only (cf. Fig. 10). For $\chi = 15°$, there is an offset in the response, as already observed in Section 4. In this case the measurement has been performed without the extensometer which may have affected the accuracy of the strain measurements. Another reason for this discrepancy might be in different boundary conditions in the experiment and the model. The change in orientation of the RVE shows the tendency of the fibers to align with the loading direction and reduce the initial off-axis angle. In the experiment, however, clamps of the testing machine introduce constraining effect, such that rotation of the fibers is reduced close to the boundaries. This fact

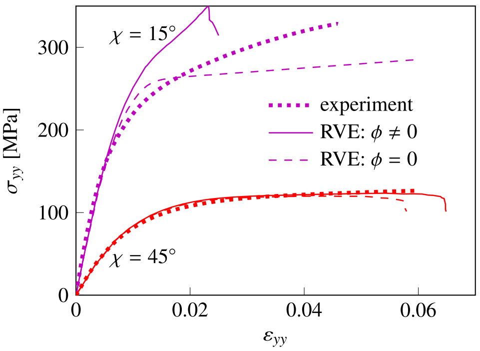

Fig. 16. Experiment compared with simulation results when the model accounts for changes in orientation ($\phi \neq 0$) and when orientation is fixed ($\phi = 0$), for two different off-axis angles.

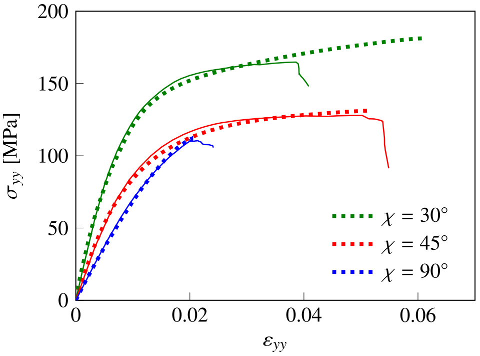

Fig. 17. Simulation (solid) versus experiment (dotted) for $\dot{\varepsilon}_{yy} = 10^{-3}$/s and different off-axis angles.

implies a mismatch between the stress state in the experiment and the model. The simulation results with the fixed RVE orientation is plotted in Fig. 16 together with the experiment and the model response for the changing orientation for $\chi = 15°$ and $\chi = 45°$. These results confirm that a small variation in the off-axis angle significantly changes the response for small off-axis angles, like $\chi = 15°$, whereas for the angle of 45° this variation has less impact on the outcome. Consequently, the effect of mismatch between the stress state of the experiment and the model increases for smaller off-axis angles. From Fig. 16 it may be hypothesized that the actual response of the specimen for $\chi = 15°$ lies between the case when the RVE freely changes orientation, and the case when this change is restrained. A full multiscale analysis similar to that performed by Gao et al. [15], with separate RVEs linked to individual macroscopic integration points accounting for macroscopic variations in the deformation, possibly provides a better match with the experiment. It may be noted that if macroscopic variations are indeed significant, the experimental results should not be interpreted as direct stress–strain measurements of the composite material. To what extent such variations are present could be checked with DIC, although that has not been done in this study.

Next, the strain-rate $\dot{\varepsilon}_{yy} = 10^{-3}$/s is considered. The simulation outcome is plotted in Fig. 17 and compared with available experiments. There is a good correspondence with the experimental observation for the angles of 45° and 90°, while for $\chi = 30°$ the simulation fails prematurely, resulting in a lower stress at failure.

In the next example $\dot{\varepsilon}_{yy} = 10^{-5}$/s is applied on the RVE. Comparison with the experiment is depicted in Fig. 18(left). The similar conclusion as for the case $\dot{\varepsilon}_{yy} = 10^{-4}$/s holds here as well. For $\chi = 45°$, the simulation ends up with a response more ductile than experimentally observed, but the stress at failure is still very close to the testing one. Results for the strain-rate of 10^{-6}/s and two different off-axis angles $\chi = 15°$ and $\chi = 90°$ are shown in Fig. 18(right). While there is a good match for 90° off-axis angle, again there is an offset for $\chi = 15°$.

In the following, three different strain-rates of: $3 \cdot 10^{-4}$/s, $3 \cdot 10^{-5}$/s and $3 \cdot 10^{-6}$/s are imposed on the RVE under two different off axis angles: 30° and 45°. The simulation outcome is plotted in Fig. 19, accompanied by the experimental results. The strain-rates considered here have not been included in the construction of the parametric curves in Fig. 11. A good agreement between the model and the experiment is obtained for $\chi = 45°$, whereas under $\chi = 30°$ a larger difference is present with a lower stress at failure than in the experiments, similar to what was observed for the other considered strain-rates. This aspect can be improved by increasing the strength $f_{\parallel}$ in Eq. (66), but that action would result in an even larger offset for $\chi = 15°$.

In Fig. 20 the computationally determined stress at failure is plotted against the corresponding strain-rate in a semilog plot, and comparison is made with the experiment. It is clear that the model matches well with the experimental observations for the angles 45° and 90°. As the off-axis angle decreases the absolute difference between the model and the observation increases. We assume

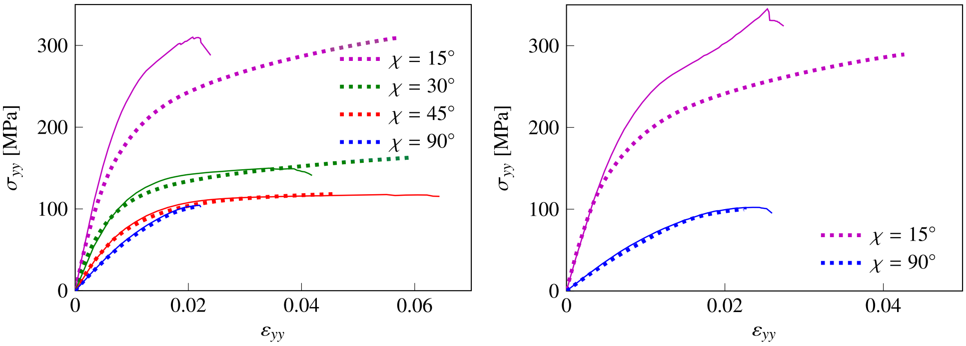

Fig. 18. Simulation (solid) versus experiment (dotted) for $\dot{\varepsilon}_{yy} = 10^{-5}$/s (left), $\dot{\varepsilon}_{yy} = 10^{-6}$/s (right), and different off-axis angles.

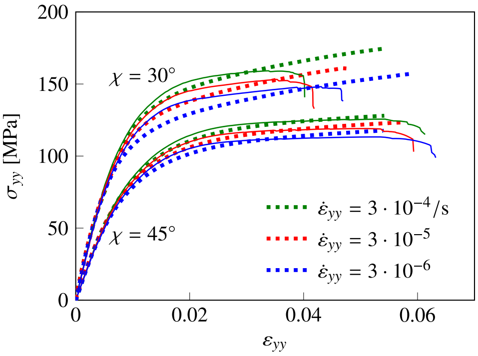

Fig. 19. Simulation (solid) versus experiment (dotted) for range of strain-rates and two different off-axis angles.

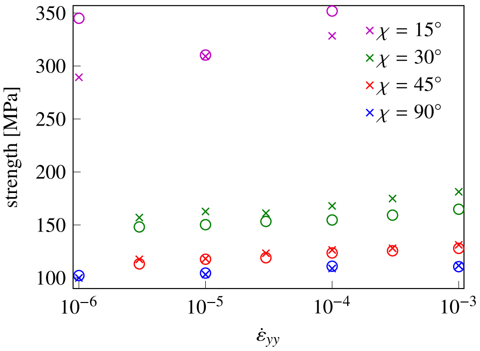

Fig. 20. Material strength determined numerically (o) and experimentally (x) under different off-axis angles.

that the biggest part of this difference is due to an inconsistent stress state in the experiment and the micromodel, whose effect increases for lower off-axis angles.

The fracturing RVE is visualized in Fig. 21 for two different strain-rates: $\dot{\varepsilon}_{yy} = 10^{-3}$/s, $\dot{\varepsilon}_{yy} = 10^{-6}$/s, and two different off-axis angles: $\chi = 45°$ and $\chi = 90°$. The contour plots indicate the distribution of the equivalent plastic strain in the polymer matrix. There is more equivalent plastic strain accumulated for $\chi = 45°$ compared to $\chi = 90°$, in line with the observation that the 45° response is much more ductile than the 90° response, see e.g. Fig. 17. Comparing the strain-rates considered, there is more equivalent plastic strain for the lower strain-rate of 10^{-6}/s for both off-axis angles.

The nonlinear response of the RVE is a competition of viscoplasticity and microcracking. To shed light on the contribution of the each source of nonlinearity, the RVE response without microcracking is plotted together with the RVE response when microcracking is included, and the comparison is made with the experiments for different off-axis angles and $\dot{\varepsilon}_{yy} = 10^{-4}$/s, see Fig. 22. As can be observed from the figure, initially the nonlinear response is not affected by microcracking and therefore is dominated by viscoplasticity. However, without microcracking the RVE response is monotonically hardening, which does not provide

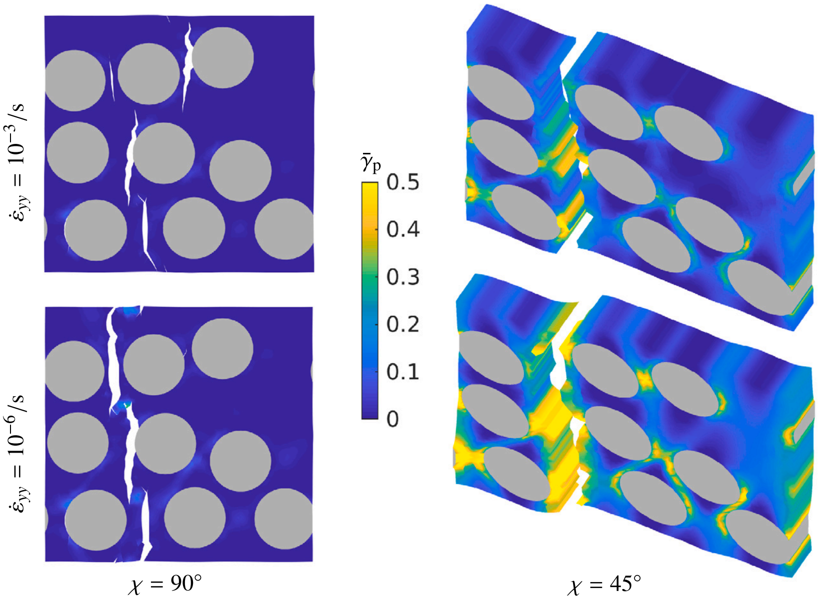

Fig. 21. Distribution of equivalent plastic strain in fracturing RVE for two different strain-rates and off-axis angles.

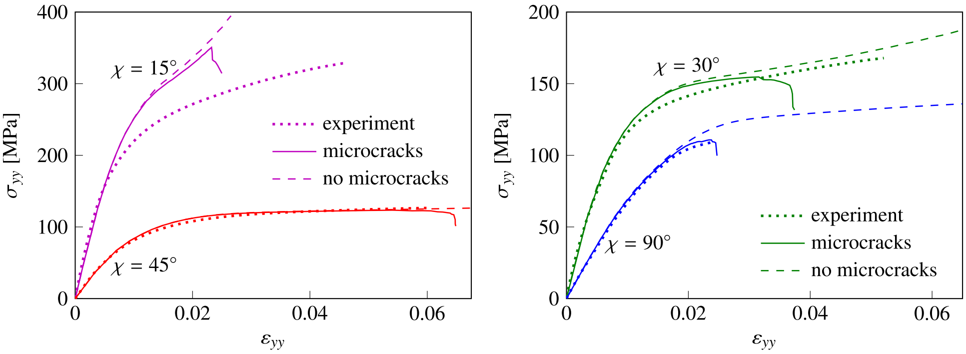

Fig. 22. Simulation with microcracking and without microcracking compared with experiments for different off-axis angles and the strain-rate of 10^{-4}/s.

an opportunity to define the failure point. Therefore, the presence of cohesive microcracks in the model is necessary to observe softening and define the material strength.

For all loading angles, the actual fracture plane forms in the post peak, i.e., in the softening regime. This process is depicted for $\chi = 45°$ and $\dot{\varepsilon}_{yy} = 10^{-4}$/s in Fig. 23, where four different states of the fracturing RVE corresponding to different points of the stress–strain curve are shown. After the material strength is reached (snapshot 1), the cohesive microcracks coalesce and deformation localizes in the fracture plane (snapshot 2), along which an actual microcrack is formed when the cohesive traction is reduced to zero locally (snapshot 3). This microcrack further propagates as more cohesive elements reach a fully damaged state along the initiated fracture plane (snapshot 4).

From Fig. 23 it is concluded that no actual microcracks with zero cohesive traction exist in the RVE when the maximum homogenized stress is reached. This fact holds true for other off-axis angles as well, and is depicted in Fig. 24, where snapshots captured at the moment of reaching the peak point in the RVE stress–strain curve are shown. The absence of cohesive segments with zero traction when the peak point is reached implies that the fracture process zone up to the failure point is larger than the RVE. Further, it is observed that the density of cohesive microcracks decreases with an increase in the off-axis angle.

The ability of the model to account for changes in the material composition is illustrated next. The strain-rate $\dot{\varepsilon}_{yy} = 10^{-4}$/s is applied on the RVE under several off-axis angles, considering the fiber volume ratio of 0.4, 0.5 and 0.6. The obtained results are shown in Fig. 25. As expected, an increase in the fiber volume ratio increases the initial stiffness of the model. Furthermore, an increase in V_f leads to a decrease in the strain at failure, implying more brittle behavior of the composite material. As for the ultimate strength, or the stress at failure, no clear trend is observed. In most of the cases, the strength increases for increasing V_f, but for $\chi = 15°$ the lowest strength is obtained with $V_f = 0.6$.

Quite often the modeling of failure processes in engineering materials by means of a cohesive zone model neglects the related geometric nonlinear effect. In this paper we have used a finite deformation framework that allows for geometric nonlinearity in

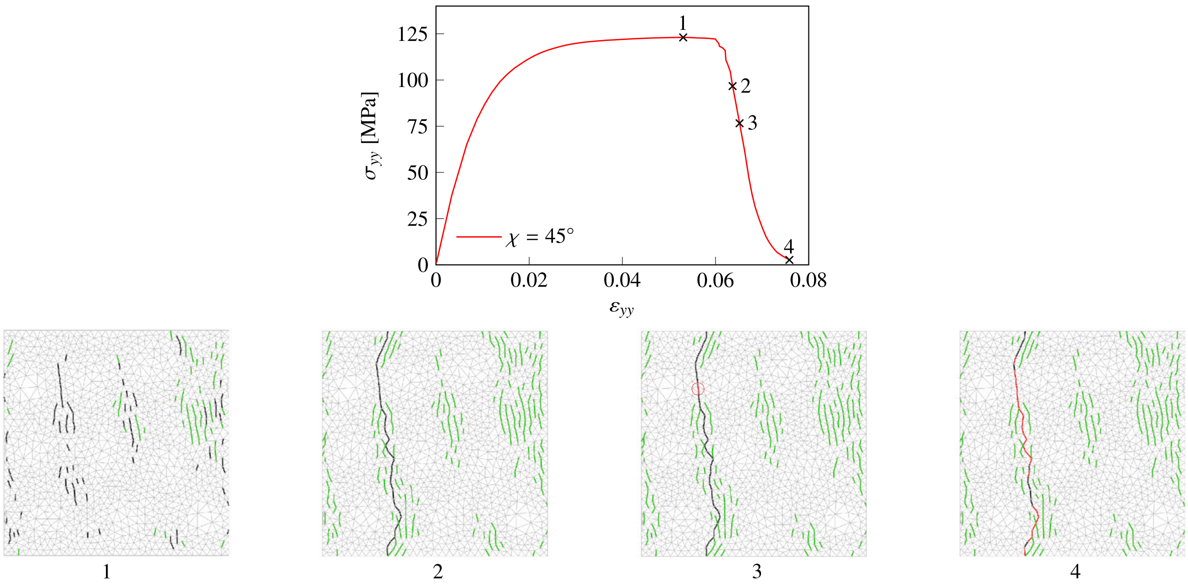

Fig. 23. Evolution of microcracking process after the material strength is reached (snapshot 1); gray color indicates uncracked element boundaries, green color stand for unloading cohesive segments, black color indicates damaging but not completely broken cohesive segments, red color represents formed microcrack with zero cohesive traction.

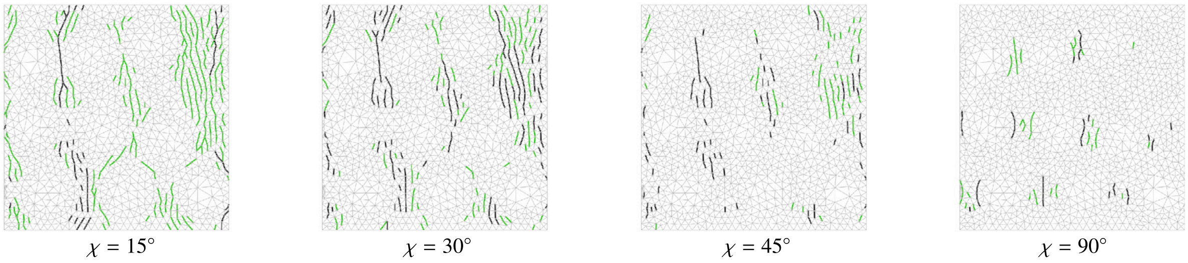

Fig. 24. Density of initiated microcracks when material strength is reached for different off-axis angles and $\dot{\varepsilon}_{yy} = 10^{-4}$/s; color scheme is the same as in Fig. 23.

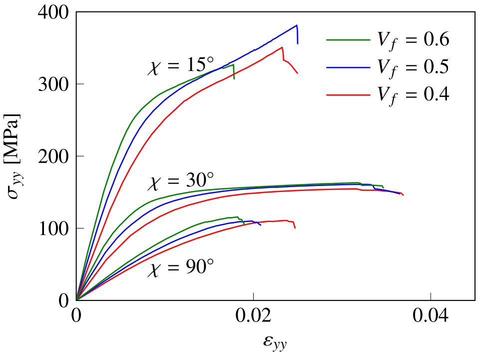

Fig. 25. Micromodel response for several fiber volume ratios, under different off-axis angles.

the cohesive zones as well, see Eq. (19). To check the effect of this on the RVE response, results as shown before that include the geometric contribution are plotted together with simulation results for which this contribution is neglected. The results are shown in Fig. 26, for $\dot{\varepsilon}_{yy} = 10^{-4}$/s and a range of off-axis angles. For the off-axis angles 30°–90° there is a small effect of the geometric nonlinear part, reflected in different strain at failure, whereas the stress at failure remains almost the same. For $\chi = 15°$ the geometric nonlinear effect is more obvious. In this case, carbon fibers bear most of the loading and a small variation in the stress and displacement field caused by the geometric nonlinear part results in obviously different stress at failure.

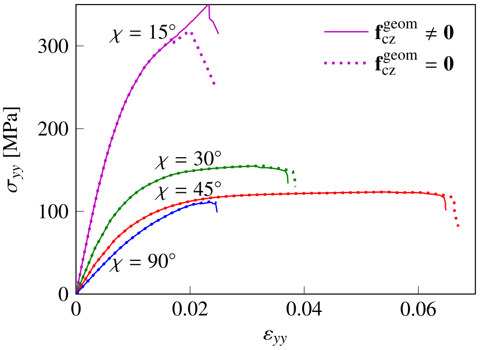

Fig. 26. Comparison of RVE response when cohesive zone geometric nonlinear effect is accounted for, and when this effect is neglected.

It should be noted that, even if the geometric contribution to the force vector was neglected, in the process of linearization there would still be a geometric contribution to the global tangent stiffness matrix. Specifically, $\mathbf{K}_{g1}$ without the factor of 2, and $\mathbf{K}_{g3}$ in Eq. (26) would be nonzero.

6. Conclusion

In this paper a 3D microscale model to simulate rate-dependent failure in unidirectional composites under off-axis loading is introduced. A prescribed macroscopic strain-rate is applied on the RVE by means of an arclength control method. The RVE model is constructed in local coordinate frame aligned with the reinforcement that may have an arbitrary orientation with respect to the global loading direction. The micromodel is defined in the finite deformation framework, and accounts for two different nonlinear processes in the polymer matrix: viscous plasticity and microcracking. The plastic deformation is represented with the Eindhoven Glassy Polymer material model, whereas a cohesive zone model represents the microcracking process. Cohesive segments are added on the fly, whenever a microcrack initiation criterion is satisfied. A new initiation criterion based on the local stress as well as the local rate of deformation state in the matrix is introduced. The fracture energy of the cohesive law depends on the mode of fracture, but is not changing for different strain-rates in the model. The presence of cohesive microcracks in the model is necessary to reach the material strength and trigger the softening response.

The ability of the RVE model to predict failure of the material is illustrated through comparison with experiments on thermoplastic UD C/PEEK composite laminates for different strain-rates and off-axis angles, at room temperature conditions. A good match is obtained for the off-axis angles 45°–90°, whereas the discrepancy between the simulation and the observation increases for the off-axis angle of 30°, and especially for 15°. A large influence of rotations of the fibers on the averaged stress–strain response is identified for the smaller off-axis angles. This observation supports the proposed explanation for the mismatch between model and test: that boundary conditions in the experiment introduce macroscopic variations in the deformation, which are not accounted for in the microscale simulations. The contour plots of the fractured RVE indicate that more equivalent plastic strain accumulates for lower strain-rates, implying the more brittle failure of the material at higher strain-rates. It has been shown that the geometric nonlinearity of the cohesive zone model has negligible impact on failure stress of C/PEEK composite system, except for $\chi = 15°$.

CRediT authorship contribution statement

Dragan Kovačević: Writing – review & editing, Writing – original draft, Visualization, Software, Methodology, Investigation, Data curation, Conceptualization. **Bharath K. Sundararajan:** Writing – review & editing, Writing – original draft, Investigation, Data curation. **Frans P. van der Meer:** Writing – review & editing, Supervision, Software, Resources, Project administration, Methodology, Funding acquisition, Conceptualization.

Declaration of competing interest

The authors declare that they have no known competing financial interests or personal relationships that could have appeared to influence the work reported in this paper.

Data availability

Data presented in this article are available at the 4TU.ResearchData repository through https://doi.org/10.4121/20065976.v1.

Acknowledgment

This research forms part of the research programme of DPI, project #811t17.

Appendix. Derivation details

To find derivatives $\partial \mathbf{Q}/\partial \mathbf{a}$ we express the transformation matrix components, Eq. (27), in terms of the initial nodal coordinates X, Y, Z and corresponding nodal displacements. Given the isoparametric mapping this is initially possible for the vectors $\mathbf{s}$ and $\mathbf{t}'$. Combining Eqs. (28)–(31) the x-component of the vector $\mathbf{s}$ is:

$$\begin{aligned} s_x = \frac{\tilde{s}_x}{\|\tilde{\mathbf{s}}\|} = \frac{1}{2}[&N_{\mathrm{A},\xi}(X_1 + u_{x1} + X_7 + u_{x7}) + N_{\mathrm{D},\xi}(X_4 + u_{x4} + X_{10} + u_{x10}) \\ &+N_{\mathrm{B},\xi}(X_2 + u_{x2} + X_8 + u_{x8}) + N_{\mathrm{E},\xi}(X_5 + u_{x5} + X_{11} + u_{x11}) \\ &+N_{\mathrm{C},\xi}(X_3 + u_{x3} + X_9 + u_{x9}) + N_{\mathrm{F},\xi}(X_6 + u_{x6} + X_{12} + u_{x12})]/\|\tilde{\mathbf{s}}\| \end{aligned} \tag{A.1}$$

Components s_y and s_z can be obtained in a similar way, replacing X respectively with Y and Z initial nodal coordinates, and also replacing u_{xi} with nodal displacements associated with y- and z-direction. In Eq. (A.1) the shape function gradients in ξ-direction are defined as:

$$\begin{aligned} &N_{\mathrm{A},\xi} = \frac{1}{4}(1-\eta)(2\xi - 1), && N_{\mathrm{D},\xi} = \frac{1}{4}(1+\eta)(2\xi + 1) \\ &N_{\mathrm{B},\xi} = -(1-\eta)\xi, && N_{\mathrm{E},\xi} = -(1+\eta)\xi \\ &N_{\mathrm{C},\xi} = \frac{1}{4}(1-\eta)(2\xi + 1), && N_{\mathrm{F},\xi} = \frac{1}{4}(1+\eta)(2\xi - 1) \end{aligned} \tag{A.2}$$

Following the same approach but combining Eqs. (28)–(30) with Eq. (32), it is possible to derive expressions for the components of the vector $\mathbf{t}'$. The x-component of this vector is:

$$\begin{aligned} t'_x = \frac{\tilde{t}'_x}{\|\tilde{\mathbf{t}}'\|} = \frac{1}{2}[&N_{\mathrm{A},\eta}(X_1 + u_{x1} + X_7 + u_{x7}) + N_{\mathrm{D},\eta}(X_4 + u_{x4} + X_{10} + u_{x10}) \\ &+N_{\mathrm{B},\eta}(X_2 + u_{x2} + X_8 + u_{x8}) + N_{\mathrm{E},\eta}(X_5 + u_{x5} + X_{11} + u_{x11}) \\ &+N_{\mathrm{C},\eta}(X_3 + u_{x3} + X_9 + u_{x9}) + N_{\mathrm{F},\eta}(X_6 + u_{x6} + X_{12} + u_{x12})]/\|\tilde{\mathbf{t}}'\| \end{aligned} \tag{A.3}$$

where the shape function gradients in η-direction are as follows:

$$\begin{aligned} &N_{\mathrm{A},\eta} = -\frac{1}{4}(\xi^2 - \xi), && N_{\mathrm{D},\eta} = \frac{1}{4}(\xi^2 + \xi) \\ &N_{\mathrm{B},\eta} = -\frac{1}{2}(1 - \xi^2), && N_{\mathrm{E},\eta} = \frac{1}{2}(1 - \xi^2) \\ &N_{\mathrm{C},\eta} = -\frac{1}{4}(\xi^2 + \xi), && N_{\mathrm{F},\eta} = \frac{1}{4}(\xi^2 - \xi) \end{aligned} \tag{A.4}$$

From Eq. (A.1) it is possible to find the derivative of the s_x component with respect to the nodal displacements:

$$s_{x,\mathbf{a}} = \frac{\partial}{\partial \mathbf{a}}\left(\frac{\tilde{s}_x}{\|\tilde{\mathbf{s}}\|}\right) = \frac{\tilde{s}_{x,\mathbf{a}}\|\tilde{\mathbf{s}}\| - \tilde{s}_x\|\tilde{\mathbf{s}}\|_{,\mathbf{a}}}{\|\tilde{\mathbf{s}}\|^2} \tag{A.5}$$

in which the derivative of the norm $\|\tilde{\mathbf{s}}\|$ is defined as:

$$\|\tilde{\mathbf{s}}\|_{,\mathbf{a}} = \frac{\tilde{s}_x\tilde{s}_{x,\mathbf{a}} + \tilde{s}_y\tilde{s}_{y,\mathbf{a}} + \tilde{s}_z\tilde{s}_{z,\mathbf{a}}}{\|\tilde{\mathbf{s}}\|} \tag{A.6}$$

Differentiation of the numerator in Eq. (A.1) with respect to the vector $\mathbf{a}$ yields the following expression:

$$\begin{aligned} \tilde{s}_{x,\mathbf{a}} = \frac{1}{2}[&N_{\mathrm{A},\xi} \quad 0 \quad 0 \quad N_{\mathrm{B},\xi} \quad 0 \quad 0 \quad N_{\mathrm{C},\xi} \quad 0 \quad 0 \ldots \\ &N_{\mathrm{D},\xi} \quad 0 \quad 0 \quad N_{\mathrm{E},\xi} \quad 0 \quad 0 \quad N_{\mathrm{F},\xi} \quad 0 \quad 0 \quad \text{repeat}]_{1\times 36(\mathrm{ndof})} \end{aligned} \tag{A.7}$$

which can be substituted in Eqs. (A.5) and (A.6). The vectors $\tilde{s}_{y,\mathbf{a}}$ and $\tilde{s}_{z,\mathbf{a}}$ from Eq. (A.6) are determined in a similar way as $\tilde{s}_{x,\mathbf{a}}$. After determining the vectors $\tilde{s}_{x,\mathbf{a}}$, $\tilde{s}_{y,\mathbf{a}}$ and $\tilde{s}_{z,\mathbf{a}}$ it is possible to calculate $s_{x,\mathbf{a}}$ with Eq. (A.5), as well as the vectors $s_{y,\mathbf{a}}$ and $s_{z,\mathbf{a}}$ with similar expressions.

For completeness, similar equations are shown for the derivative of $\mathbf{t}'$ vector x-component:

$$t'_{x,\mathbf{a}} = \frac{\partial}{\partial \mathbf{a}}\left(\frac{\tilde{t}'_x}{\|\tilde{\mathbf{t}}'\|}\right) = \frac{\tilde{t}'_{x,\mathbf{a}}\|\tilde{\mathbf{t}}'\| - \tilde{t}'_x\|\tilde{\mathbf{t}}'\|_{,\mathbf{a}}}{\|\tilde{\mathbf{t}}'\|^2} \tag{A.8}$$

$$\|\tilde{\mathbf{t}}'\|_{,\mathbf{a}} = \frac{\tilde{t}'_x\tilde{t}'_{x,\mathbf{a}} + \tilde{t}'_y\tilde{t}'_{y,\mathbf{a}} + \tilde{t}'_z\tilde{t}'_{z,\mathbf{a}}}{\|\tilde{\mathbf{t}}'\|} \tag{A.9}$$

$$\begin{aligned} \tilde{t}'_{x,\mathbf{a}} = \frac{1}{2}[&N_{\mathrm{A},\eta} \quad 0 \quad 0 \quad N_{\mathrm{B},\eta} \quad 0 \quad 0 \quad N_{\mathrm{C},\eta} \quad 0 \quad 0 \ldots \\ &N_{\mathrm{D},\eta} \quad 0 \quad 0 \quad N_{\mathrm{E},\eta} \quad 0 \quad 0 \quad N_{\mathrm{F},\eta} \quad 0 \quad 0 \quad \text{repeat}]_{1\times 36(\mathrm{ndof})} \end{aligned} \tag{A.10}$$

Now that the vectors $s_{i,\mathbf{a}}$ and $t'_{i,\mathbf{a}}$ are fully defined, where $i = x, y, z$, they can be used to define the change in the unit normal vector with nodal displacements. Differentiating Eq. (33) with respect to **a** leads to:

$$\frac{\partial \mathbf{n}}{\partial \mathbf{a}} = \begin{bmatrix} n_{x,\mathbf{a}} \\ n_{y,\mathbf{a}} \\ n_{z,\mathbf{a}} \end{bmatrix} = \begin{bmatrix} s_{y,\mathbf{a}} t'_z + s_y t'_{z,\mathbf{a}} - s_{z,\mathbf{a}} t'_y - s_z t'_{y,\mathbf{a}} \\ s_{z,\mathbf{a}} t'_x + s_z t'_{x,\mathbf{a}} - s_{x,\mathbf{a}} t'_z - s_x t'_{z,\mathbf{a}} \\ s_{x,\mathbf{a}} t'_y + s_x t'_{y,\mathbf{a}} - s_{y,\mathbf{a}} t'_x - s_y t'_{x,\mathbf{a}} \end{bmatrix} \tag{A.11}$$

Applying the same differentiation procedure in Eq. (34) yields:

$$\frac{\partial \mathbf{t}}{\partial \mathbf{a}} = \begin{bmatrix} t_{x,\mathbf{a}} \\ t_{y,\mathbf{a}} \\ t_{z,\mathbf{a}} \end{bmatrix} = \begin{bmatrix} n_{y,\mathbf{a}} s_z + n_y s_{z,\mathbf{a}} - n_{z,\mathbf{a}} s_y - n_z s_{y,\mathbf{a}} \\ n_{z,\mathbf{a}} s_x + n_z s_{x,\mathbf{a}} - n_{x,\mathbf{a}} s_z - n_x s_{z,\mathbf{a}} \\ n_{x,\mathbf{a}} s_y + n_x s_{y,\mathbf{a}} - n_{y,\mathbf{a}} s_x - n_y s_{x,\mathbf{a}} \end{bmatrix} \tag{A.12}$$

Eqs. (A.11) and (A.12), together with the vectors $s_{i,\mathbf{a}}$ are finally used in Eq. (35) to construct $\partial \mathbf{Q}/\partial \mathbf{a}$.

References

[1] Alderliesten R. Introduction to aerospace structures and materials. Delft University of Technology; 2018.

[2] Azzi VD, Tsai SW. Anisotropic strength of composites. Exp Mech 1965;5(9):283–8.

[3] Tsai SW, Wu EM. A general theory of strength for anisotropic materials. J Compos Mater 1971;5(1):58–80.

[4] Hashin Z, Rotem A. A fatigue failure criterion for fiber reinforced materials. J Compos Mater 1973;7(4):448–64.

[5] Puck A, Schürmann H. Failure analysis of FRP laminates by means of physically based phenomenological models. Compos Sci Technol 2002;62(12):1633–62.

[6] Dávila CG, Camanho PP, Rose CA. Failure criteria for FRP Laminates. J Compos Mater 2005;39(4):323–45.

[7] Camanho PP, Arteiro A, Melro AR, Catalanotti G, Vogler M. Three-dimensional invariant-based failure criteria for fibre-reinforced composites. Int J Solids Struct 2015;55:92–107.

[8] Sun Q, Zhou G, Meng Z, Guo H, Chen Z, Liu H, et al. Failure criteria of unidirectional carbon fiber reinforced polymer composites informed by a computational micromechanics model. Compos Sci Technol 2019;172:81–95.

[9] Totry E, González C, LLorca J. Prediction of the failure locus of C/PEEK composites under transverse compression and longitudinal shear through computational micromechanics. Compos Sci Technol 2008;68(15):3128–36.

[10] Vogler TJ, Kyriakides S. Inelastic behavior of an AS4/PEEK composite under combined transverse compression and shear. Part I: Experiments. Int J Plast 1999;15(8):783–806.

[11] Vaughan TJ, McCarthy CT. A micromechanical study on the effect of intra-ply properties on transverse shear fracture in fibre reinforced composites. Composites A 2011;42(9):1217–28.

[12] Sharma A, Daggumati S, Gupta A, Van Paepegem W. On the prediction of the bi-axial failure envelope of a UD CFRP composite lamina using computational micromechanics: effect of microscale parameters on macroscale stress–strain behavior. Compos Struct 2020;251:112605.

[13] Bhuiyan FH, Sanei SHR, Fertig RS. Predicting variability in transverse effective elastic moduli and failure initiation strengths in UD composite microstructures due to randomness in fiber location and morphology. Compos Struct 2020;237:111887.

[14] Bai X, Bessa MA, Melro AR, Camanho PP, Guo L, Liu WK. High-fidelity micro-scale modeling of the thermo-visco-plastic behavior of carbon fiber polymer matrix composites. Compos Struct 2015;134:132–41.

[15] Gao J, Shakoor M, Domel G, Merzkirch M, Zhou G, Zeng D, et al. Predictive multiscale modeling for unidirectional carbon fiber reinforced polymers. Compos Sci Technol 2020;186:107922.

[16] Sato M, Shirai S, Koyanagi J, Ishida Y, Kogo Y. Numerical simulation for strain rate and temperature dependence of transverse tensile failure of unidirectional carbon fiber-reinforced plastics. J Compos Mater 2019;53(28–30):4305–12.

[17] Govaert LE, Schellens HJ, Thomassen HJM, Smit RJM, Terzoli L, Peijs T. A micromechanical approach to time-dependent failure in off-axis loaded polymer composites. Composites A 2001;32(12):1697–711.

[18] Reinoso J, Paggi M. A consistent interface element formulation for geometrical and material nonlinearities. Comput Mech 2014;54(6):1569–81.

[19] Camacho GT, Ortiz M. Computational modelling of impact damage in brittle materials. Int J Solids Struct 1996;33(20):2899–938.

[20] Kovačević D, Van der Meer FP. Strain-rate based arclength model for nonlinear microscale analysis of unidirectional composites under off-axis loading. Int J Solids Struct 2022;250:111697.

[21] Erartsın O, Van Drongelen M, Govaert LE. Identification of plasticity-controlled creep and fatigue failure mechanisms in transversely loaded unidirectional thermoplastic composites. J Compos Mater 2021;55(14):1947–65.

[22] Koerber H, Xavier J, Camanho PP. High strain rate characterisation of unidirectional carbon-epoxy IM7-8552 in transverse compression and in-plane shear using digital image correlation. Mech Mater 2010;42(11):1004–19.

[23] Sun CT, Chung I. An oblique end-tab design for testing off-axis composite specimens. Composites 1993;24(8):619–23.

[24] Van der Meer FP. Micromechanical validation of a mesomodel for plasticity in composites. Eur J Mech A Solids 2016;60:58–69.

[25] Wells GN, De Borst R, Sluys LJ. A consistent geometrically non-linear approach for delamination. Internat J Numer Methods Engrg 2002;54(9):1333–55.

[26] Zhi J, Chen B-Y, Tay T-E. Geometrically nonlinear analysis of matrix cracking and delamination in composites with floating node method. Comput Mech 2019;63(2):201–17.

[27] Ortiz M, Pandolfi A. Finite-deformation irreversible cohesive elements for three-dimensional crack-propagation analysis. Int J Numer Methods Eng 1999;44(9):1267–82.

[28] Belytschko T, Liu WK, Moran B, Elkhodary K. Nonlinear finite elements for continua and structures. John Wiley & Sons; 2014.

[29] Eyring H. Viscosity, plasticity, and diffusion as examples of absolute reaction rates. J Chem Phys 1936;4(4):283–91.

[30] Van Breemen LCA, Klompen ETJ, Govaert LE, Meijer HEH. Extending the EGP constitutive model for polymer glasses to multiple relaxation times. J Mech Phys Solids 2011;59(10):2191–207.

[31] Tervoort TA, Smit RJM, Brekelmans WAM, Govaert LE. A constitutive equation for the elasto-viscoplastic deformation of glassy polymers. Mech Time Depend Mater 1997;1(3):269–91.

[32] Klompen ETJ, Govaert LE. Nonlinear viscoelastic behaviour of thermorheologically complex materials. Mech Time Depend Mater 1999;3(1):49–69.

[33] Klompen ETJ, Engels TAP, Govaert LE, Meijer HEH. Modeling of the postyield response of glassy polymers: influence of thermomechanical history. Macromolecules 2005;38(16):6997–7008.

[34] Bonet J, Burton AJ. A simple orthotropic, transversely isotropic hyperelastic constitutive equation for large strain computations. Comput Methods Appl Mech Engrg 1998;162(1):151–64.

[35] Miyagawa H, Sato C, Mase T, Drown E, Drzal LT, Ikegami K. Transverse elastic modulus of carbon fibers measured by raman spectroscopy. Mater Sci Eng A 2005;412(1):88–92.
[36] Liu Y, Van der Meer FP, Sluys LJ, Ke L. Modeling of dynamic mode I crack growth in glass fiber-reinforced polymer composites: Fracture energy and failure mechanism. Eng Fract Mech 2021;243:107522.
[37] Van der Meer FP, Sluys LJ. A phantom node formulation with mixed mode cohesive law for splitting in laminates. Int J Fract 2009;158(2):107.
[38] Hille TS, Suiker ASJ, Turteltaub S. Microcrack nucleation in thermal barrier coating systems. Eng Fract Mech 2009;76(6):813–25.
[39] Christensen RM. The theory of materials failure. Oxford University Press; 2013.
[40] Bonet J, Wood RD. Nonlinear continuum mechanics for finite element analysis. Cambridge University Press; 1997.